

Relationship between a Weakening Cold Front, Misocyclones, and Cloud Development on 10 June 2002 during IHOP

NETTIE R. ARNOTT AND YVETTE P. RICHARDSON

The Pennsylvania State University, University Park, Pennsylvania

JOSHUA M. WURMAN

Center for Severe Weather Research, Boulder, Colorado

ERIK M. RASMUSSEN

National Severe Storms Laboratory, Norman, Oklahoma

(Manuscript received 3 December 2004, in final form 21 June 2005)

ABSTRACT

The finescale structure and evolution of a cold front in the presence of small-scale circulations are examined using overdetermined dual-Doppler syntheses of mobile radar data along with thermodynamic data and cloud imagery collected on 10 June 2002 during the International H₂O Project (IHOP). Linear clear-air reflectivity maxima and open cellular convection intersect the cold front, causing spatial variations in convergence along the front. Small-scale vertical vorticity maxima (misocyclones) often are coincident with these intersections and are associated with vertical velocity maxima.

Throughout the deployment, trajectory analyses indicate that parcels entering the frontal circulation travel predominately in the along-front direction. During the first hour of the deployment, upward motion is nearly continuous along the front. Consequently, parcels remain in regions of upward motion as they move along the front, and many eventually ascend to cloud base. In response, a line of cumulus clouds develops along the front.

Later in the deployment, however, enhanced warming behind the cold front causes the frontal circulation to weaken. Small-scale features such as misocyclones play a larger role in organizing upward motion along the front than when the front was stronger. Misocyclones contort the weakened cold front and are associated with kinks in radar reflectivity and fractures in upward motion. Parcels moving along the front now experience regions of both upward and downward forcing due to this fracturing. Hence, many of these parcels do not retain upward motion long enough to reach cloud base, and clouds along the cold front dissipate in the dry air above the boundary layer. Parcels that remain coincident with upward motion maxima, such as those maxima associated with misocyclones, however, often still reach the top of the radar domain and presumably cloud base.

1. Introduction

Predicting if, where, and when cumulonimbus clouds develop is a challenge for forecasters and for computer models alike. Forecasters struggle with data that are too coarse to pinpoint where storms will form before the clouds are observed by radar or satellite. Furthermore, exactly which small-scale features forecasters

should track is unknown due to limited understanding of the processes governing convection initiation (CI). Likewise, numerical models demonstrate much lower skill in summer quantitative precipitation forecasts (QPF) than in winter QPF (Parsons et al. 2001). One reason for this low skill is the typical occurrence of convective events on scales less than the grid spacing for operational models. Hence, the processes forcing these events must be parameterized. Cloud-resolving models have finer grid spacing but incomplete available measurements of the boundary layer water vapor and wind fields, which are crucial for predicting convection and precipitation (Parsons et al. 2001). Hence, to im-

Corresponding author address: Yvette P. Richardson, Dept. of Meteorology, The Pennsylvania State University, 503 Walker Building, University Park, PA 16802.
E-mail: yrichardson@psu.edu

prove CI forecasts, we must first understand the processes governing CI and then we can determine which data forecasters and models require and on what scales those data are necessary.

Since the Thunderstorm Project of the 1940s, forecasters have recognized that zones of enhanced convergence, given adequate thermodynamic instability, are favorable for initiating convection (Byers and Rodebush 1948). Enhanced convergence not only suggests the presence of enhanced upward motion, but also often indicates a deepening of the moist layer by vertical advection, priming the environment for CI (e.g., Wilson et al. 1992). Consequently, many CI studies use enhanced convergence to diagnose the CI potential along a variety of atmospheric boundaries.

Past research has identified that intersections of convergence boundaries are particularly favorable CI locations. For instance, convection may be initiated at intersections such as the sea breeze with gust fronts and gusts fronts with horizontal convective rolls (HCRs) (e.g., Fankhauser et al. 1995; Kingsmill 1995; Wilson and Megenhardt 1997), the dryline with other mesoscale convergence zones (e.g., Hane et al. 1997, 2002), the Denver convergence zone with HCRs (e.g., Lee et al. 1991; Wilson and Schreiber 1986; Wilson et al. 1992), and gust fronts with a cold front (Weaver and Nelson 1982). Likewise, Weckwerth and Wakimoto (1992) document CI along a thunderstorm gust front and additional shallow cumulus formation at intersections of Kelvin–Helmholtz waves with gravity waves.

Ziegler et al. (1997) and Ziegler and Rasmussen (1998) stress the importance of *deep* moist mesoscale convergence zones in initiating deep convection. In other words, the dwell time of a parcel within the moist convergence associated with a boundary is key to initiating convection. If parcels are able to stay in deep moist convergence up to the LFC, convection likely will be initiated. If parcels leave the deep moist convergence before reaching the LFC, however, the ability of the boundary to initiate convection is decreased. Therefore, it is important to understand how the pattern of upward forcing along a mesoscale boundary affects parcel paths and to understand what factors may govern this organization. High spatial and temporal resolution kinematic and thermodynamic data are required in order to understand these small-scale along-boundary inhomogeneities that may make one portion of a boundary favorable for CI, but another portion unfavorable.

Some progress has been made in documenting along-boundary inhomogeneities that may influence CI along a boundary. For example, many studies have found that intersections of a boundary with HCRs are favorable locations for cloud development (e.g., Atkins et al.

1995; Fankhauser et al. 1995; Kingsmill 1995; Wilson and Megenhardt 1997; Lee et al. 1991; Wilson and Schreiber 1986; Wilson et al. 1992). Locally, HCR updraft branches are often associated with deeper moisture and lower LCLs (Weckwerth et al. 1996).

In addition, HCR–boundary intersections are associated with updrafts and vorticity maxima. For example, Atkins et al. (1995) note that updrafts along the sea breeze front tilt the HCRs 20° from the horizontal, locally deepening upward motion and enhancing any clouds that are advected over the intersection. Further, by tilting the horizontal vorticity associated with the HCRs into the vertical, small (40 m–4 km) vertical vorticity maxima, or misocyclones, are produced.

Alternatively, Wilson et al. (1992) found that intersections of HCRs with the Denver convergence zone created an enhanced updraft and subsequently stretched ambient vertical vorticity, producing a vertical vorticity maximum. This enhanced updraft also developed a cloud at the intersection point.

Misocyclones can form in areas without boundary intersections through horizontal shearing instability as well (Kingsmill 1995; Lee and Wilhelmson 1997). In this case, no misoanticyclone is produced, and the role of HCR updrafts may be to stretch and amplify the vorticity associated with these misocyclones. Regardless of the formation mechanism, misocyclones are associated with nearby vertical velocity maxima that could be expected to be favored regions for CI (Marquis et al. 2004). Indeed, in all of the studies cited except Kingsmill (1995), misocyclones are preferred locations for cloud development and/or deepening. Perhaps the dwell time of parcels within the misocyclone-associated vertical velocity maxima, which may depend on other characteristics of the boundary, is important in determining whether or not the vertical velocity maxima will be favorable for cloud development. Further, it is unclear how misocyclones may influence the organization of upward forcing along an *evolving* boundary and how this influence affects the dwell time of parcels within regions of upward motion and, hence, the ability of the boundary as a whole to initiate convection. Examining parcel trajectories is a useful way to more precisely determine if these boundaries have the potential to lift parcels to the LFC.

Even though convergence boundaries and intersections of boundaries are favorable locations for storm development, not all boundaries and intersections initiate deep moist convection, even when the convective inhibition (CIN) is very small (Ziegler and Rasmussen 1998). Furthermore, under similar synoptic-scale conditions, some boundaries (or a portion of a boundary) may initiate convection while other boundaries (or an-

other portion of the same boundary) may not. Moisture variability may be one controlling factor. Another may be the horizontal vorticity balance across the boundary if the boundary is approximately two-dimensional (Rotunno et al. 1988, hereafter RKW; Lee et al. 1991; Wilson et al. 1992; Wilson and Megenhardt 1997). This vorticity balance has been theorized to aid in the development of an erect updraft. Spatial variations of the horizontal vorticity balance across a boundary may help explain why convection is initiated along one portion of a boundary and not along another.

Kinematic data with finer temporal and spatial resolution than in previous studies are required to address how misocyclones influence the organization of upward forcing along an evolving boundary and how this influence affects the dwell time of parcels in regions of upward motion. Finer resolution also affords an examination of spatial and temporal variations in other kinematic properties such as the horizontal vorticity balance across the boundary. Ideally suited to the collection of high-resolution kinematic data, Doppler weather radar can detect convergence lines prior to cloud development as thin lines of enhanced reflectivity and as regions of wind shear (Wilson and Schreiber 1986) because insects and airborne particulates scatter radiation back to the radar. This allows for both clear-air reflectivity and radial wind measurements of convergence lines (Wilson et al. 1994). Past studies have examined lines with temporal resolution of typically 5 min or more, but some current mobile radars can acquire volumes of data in only 90 s. Further, because the mobile radars can deploy close to the target, data spacing is reduced.

In this study we focus on 10 June 2002, when a quasi-stationary cold front, a secondary convergence boundary, boundary layer linear reflectivity maxima, cellular convection, and misocyclones were observed by four mobile ground-based Doppler radars deployed within 15 km of the cold front, allowing for high spatial and temporal resolution volumes. Boundary layer thermodynamic measurements of these features were collected also. Using the mobile Doppler radar data with aircraft, sounding, and photogrammetry data, this case study documents the structure and evolution of the cold front and embedded misocyclones along the front and examines how these features influenced the associated cumulus cloud field.

This study is unique in that observations of a convergence zone potentially favorable for initiating convection with misocyclones along it are studied with high-resolution radar and cloud data. Not only does high spatial resolution enhance details in the overdetermined dual-Doppler syntheses, but the high temporal

resolution allows parcel trajectories to be computed, unlike many previous CI studies. Additionally, a marked dissipation in the areal extent of cumulus growth was observed along the cold front. Misocyclones are found to play an important role in the organization of the vertical velocity field and subsequent cloud development along the boundary. This sequence of events has not been documented before with such fine resolution and should enhance understanding of the nature of convergence boundaries and the influence of small-scale features on the boundaries. Section 2 describes the data and methods used to analyze the radar data. The case study is presented in section 3 and conclusions regarding those observations are discussed in section 4.

2. Data collection and analysis

Although researchers have identified characteristics that can favor CI, it remains a significant forecasting challenge. Reasons for this include 1) forecasters must rely on coarse-resolution operational data, and hence have difficulty detecting the inhomogeneities along convergence zones responsible for CI; 2) the formation and evolution of boundaries that can initiate convection are understood poorly; 3) high spatial and temporal resolution observations of the factors governing the complete processes during CI are not available to verify various theories.

To overcome these deficiencies, the International H₂O Project (IHOP) was conducted in the southern Great Plains for 6 weeks during May and June 2002. IHOP consisted of four primary research focus areas: water vapor instrumentation, boundary layer evolution, quantitative precipitation forecasts, and convection initiation (Weckwerth et al. 2004). In hope of acquiring high-resolution kinematic and thermodynamic data near CI, many different observing platforms including mobile ground-based and airborne Doppler radars, mobile surface and airborne probes, lidars, soundings, and profilers targeted regions over which CI was forecast to occur, with special emphasis on approximately 20 km × 20 km areas designated as intensive observation regions (IORs).

On 10 June 2002, efforts focused on CI in central Kansas with four ground-based mobile radars forming the corners of the IOR. Because overdetermined dual-Doppler data (hereafter, “multi-Doppler data”) are available outside this region, the IOR refers hereafter to the grid domain on which data subsequently are analyzed (Fig. 1). The Naval Research Laboratory (NRL) P-3 and University of Wyoming King Air made several passes over the IOR collecting in situ thermodynamic

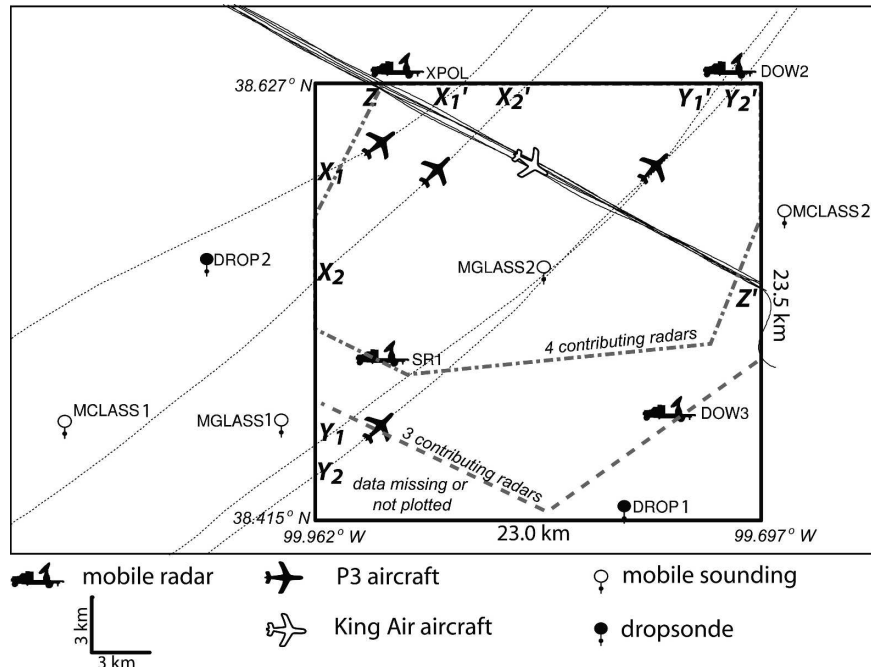


FIG. 1. Intensive observation region for 10 Jun 2002. Data were collected in this region between 1928 and 2118 UTC. The region bounded by the dashed lines is the approximate area in which three radars contribute to the syntheses. Similarly, the region bounded by the dash-dot lines is the approximate area in which four radars contribute to the syntheses. Outside these areas, data are sparse and are not plotted.

and kinematic data. Additionally, a National Severe Storms Laboratory (NSSL) Mobile Cross-Chain Loran Atmospheric Sounding System (M-CLASS) and National Center for Atmospheric Research (NCAR) Mobile GPS/Loran Atmospheric Sounding System (M-GLASS) launched soundings within the IOR. Other data sources include the NOAA/NSSL mobile mesonet, cloud photographs, and high-resolution (1 km) satellite data.

a. Radar editing

Two Doppler on Wheels (DOW) radars (Wurman et al. 1997) and the mobile Doppler X-band polarimetric (XPOL) radar (Wurman 2001) (3-cm wavelength, 0.95° beamwidth), and the Shared Mobile Atmospheric Research and Teaching Radar (SMART-Radar) (5-cm wavelength, 1.5° beamwidth) (Biggerstaff and Guynes 2000) collected data between 1928 and 2118 UTC. Each radar scanned a $\sim 180^\circ$ sector toward the center of the IOR. The DOW and XPOL radars scanned elevations from 0.5° to 14.4° above the horizontal with 0.5° increments below 3.5° and approximately 1.0° increments above 3.5° . They collected a volume every 90 s. The SMART-Radar collected a volume every 180 s at elevation angles of 0.5° , 0.8° , 1.7° , 2.9° , 4.4° , 6.0° , 7.7° ,

9.5° , 11.5° , 13.7° , and 21.7° . To minimize second-trip echoes, DOW2 and DOW3 frequently changed the pulse repetition frequency (PRF), leading to varying degrees of oversampling in the azimuthal direction. Typical beamwidth at the center of the IOR is 200 m, but, when accounting for oversampling, the data spacing is reduced to about 130 m. Typical data spacing in the radial direction is 75 m.

The radars typically were synchronized so that each volume was observed by the radars over the same period. Because CI studies require observations before precipitation forms, clear-air returns are needed. All four radars can detect clear-air returns given a sufficient insect population, and, on this particular day, sufficient returns were present up to at least 1.5 km above ground level (AGL) and a radar range of 20 km.

A semiautomated approach using NCAR's SOLO software program (Oye et al. 1995) was undertaken to remove ground clutter echoes from the data based on concurrent high reflectivity and low velocity. The Barger-Brown (1980) scheme was used for most of the velocity dealiasing. Manual dealiasing, however, was required where the automated scheme failed, such as near large velocity gradients in the radial direction.

Before the radar data can be synthesized on a com-

mon earth-relative grid, several corrections must be applied. First, because mobile radar data are collected in a truck-relative coordinate system, the data azimuths must be made earth-relative by adding an offset based on the truck orientation. This offset is found using a newly implemented solar alignment technique customized for mobile radar platforms (Arnott et al. 2003). Because the XPOL and the SMART-Radar did not perform an alignment scan on 10 June 2002, ground clutter echoes were matched with known tower locations and power lines to determine the radar orientation.

Next, a correction was applied to account for movement of features during the time required to collect the volume such that the resulting volume represents data valid at a central time. Without this correction, features will obtain an artificial tilt in the direction of motion. For a reference frame speed of greater than 2 m s^{-1} , this error will exceed the grid spacing of this study; thus, we correct for this distortion by moving the observations to their location at the center time of the volume using the velocity of the most steady reference frame (U_0, V_0) as defined by Matejka (2002).

Six (U_0, V_0) pairs of approximately $(3, 5) \text{ m s}^{-1}$ were determined and applied for approximately 20-min intervals. We estimate the error in (U_0, V_0) to be less than 0.5 m s^{-1} , which represents a maximum displacement error of 22.5 m, much less than the grid spacing of 100 m. We account for vertical changes in the reference frame velocity by determining (U_0, V_0) pairs at three vertical levels and linearly interpolating between those levels.

b. Objective analysis and multi-Doppler synthesis

Once the data were transformed to a common reference time, REORDER software (Oye and Case 1995) was used to create Barnes objective analyses (Barnes 1964) for all four radars. Koch et al. (1983) propose the following criteria for analysis grid spacing Δg :

$$\frac{\Delta d}{3} \leq \Delta g \leq \frac{\Delta d}{2}, \tag{1}$$

where Δd is the data spacing. The upper limit is imposed to resolve the observed wavelengths sufficiently on the grid, and the lower limit is imposed to minimize noise in derivative fields. Because azimuthal and vertical data spacing depend on distance from the radar and vary with each radar, no single grid spacing will satisfy (1) at all ranges and times. Thus, one must optimize the grid spacing such that features in the primary interest region are well resolved while not compromising the resolution too severely closer to the radar or creating

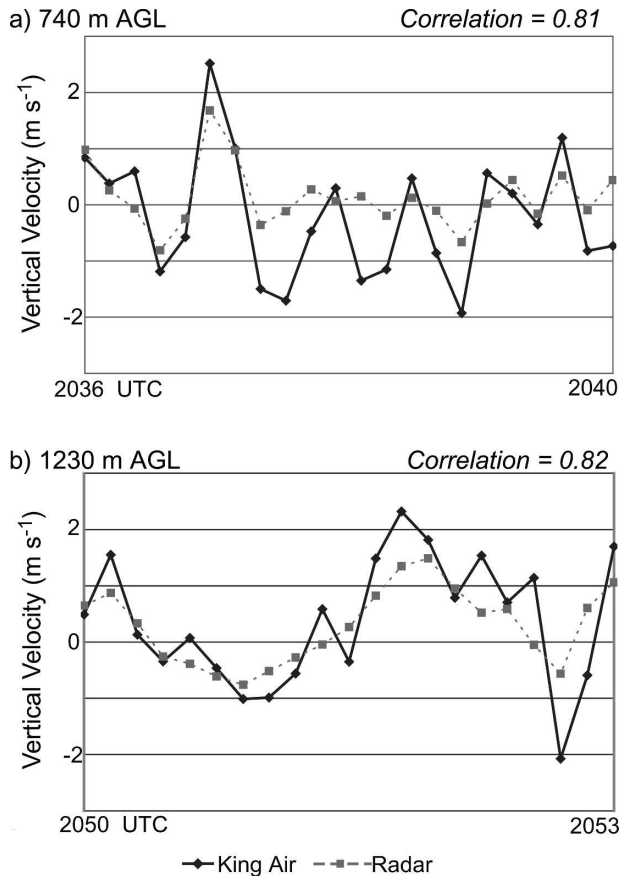


FIG. 2. Time series of vertical velocity observed by the King Air compared to vertical velocities calculated from the multi-Doppler syntheses indicating the agreement between the two data sources.

very noisy derivative fields farther from the radar. We chose Δd based on the 1° separation between elevation scans and on the beamwidth at the average distance between a radar and the center of the primary interest region, leading to 100-m grid spacing in $x, y,$ and z .

The Barnes smoothing parameter, κ , was based on the Pauley and Wu (1990) recommendation that $\kappa = (1.33\Delta d)^2 = 0.264 \text{ km}^2$. If κ is too large, important features will be smoothed out, whereas if it is too small, wavelengths less than twice the data spacing will not be damped sufficiently.

Finally, NCAR's Custom Editing and Display of Reduced Information in Cartesian Space (CEDRIC) software was used to produce multi-Doppler syntheses. Kessinger et al.'s (1987) overdetermined dual-Doppler approach was applied to estimate the horizontal wind components using four radars, and an iterative technique was subsequently used to determine the vertical velocity from the mass continuity equation. In particular, beginning at the surface with vertical velocity, $w = 0 \text{ m s}^{-1}$, w at the next level (level 2) is estimated from

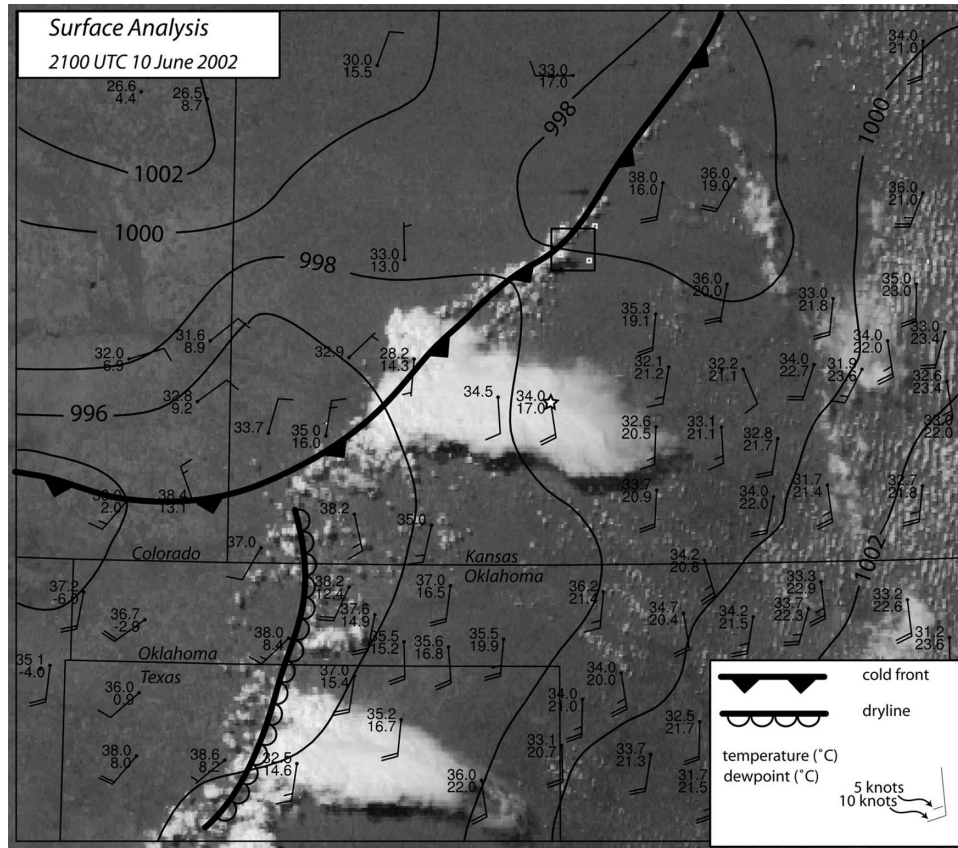


FIG. 3. Location of the cold front observed on 10 Jun 2002. Mean sea level pressure is contoured every 2 mb. Small box in west-central Kansas depicts the bounds on subsequent analyses: the IOR. Small squares are the mobile radar locations and the southwesternmost radar is located at Ness City, KS. The station with the star is Dodge City, KS.

integration of the layer-average divergence. This estimate for w is used to adjust the estimated horizontal divergence at level 2, and a new estimate for w at level 2 is obtained. This iteration continues until a domain-wide average of the change in the density-weighted vertical velocity between iterations reaches a specified cutoff ($0.01 \text{ kg m}^{-2} \text{ s}^{-1}$). Because data are sparse in the southern region of the IOR, only regions to which three or four radars contribute to the syntheses are plotted in forthcoming figures. The regions with three or four contributing radars vary slightly during the deployment, but the approximate areas are outlined in Fig. 1.

Time series of vertical velocity observed by the King Air are compared to time series of vertical velocity calculated in the multi-Doppler syntheses (Fig. 2). Comparing in situ observations with radar-derived quantities is not straightforward because radar quantities are representative over the radar volume time and over a grid cell. The ground-relative speed of the King Air was approximately 100 m s^{-1} , such that the King Air moved roughly one grid length (100 m) every second. Hence,

the 1-Hz data recorded by the King Air has similar spatial resolution as the synthesized radar data. The radar data, however, represent a 90-s period. Thus, some time averaging of the King Air 1-Hz data is warranted and we applied a 10-s (1 km) running mean. Further difficulties in the comparison arise from inherent damping of small wavelength amplitudes when objectively analyzing radar data to aircraft point measurements. Nevertheless, observed and radar-derived vertical velocities compare well and are highly correlated (see Fig. 2). Thus, we are confident that the vertical velocities in forthcoming analyses are reasonable.

3. 10 June 2002 case study

a. Synoptic conditions

A slowly sagging cold front was draped across the Great Plains into southern Colorado on the afternoon of 10 June 2002 (Fig. 3). Although the temperature and moisture gradients across the front are small, the wind shift from southerly to north-northeasterly clearly de-

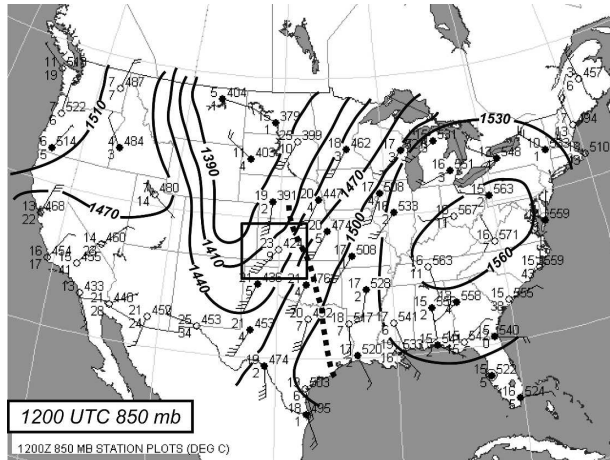


FIG. 4. An 850-mb height analysis for 10 Jun 2002 showing the location of the moisture axis (dashed line) and southwesterly flow over central Kansas. Black contours are geopotential heights in meters. Winds are in knots. Station data follow convention. The black box indicates the bounds on the surface analysis in Fig. 3.

picts its location. At 850 mb, a trough west of Kansas produced strong south-southwest flow over the analysis region and the moisture axis extended across central Kansas (Fig. 4, valid at 1200 UTC). By 0000 UTC on 11 June 2002, the moisture axis pushed into eastern Kansas (not shown).

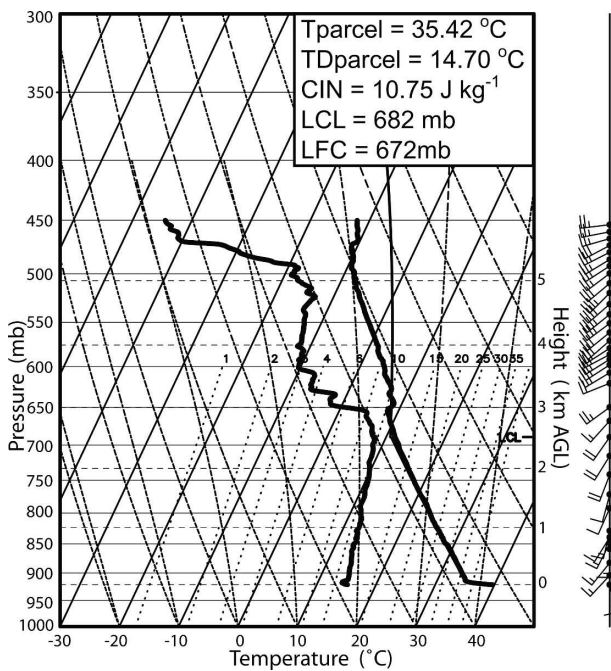


FIG. 5. Sounding on a skew T for M-GLASS2 at 2044 UTC. The parcel path and calculated indices are shown for a parcel with a surface temperature of 35.42°C . The abbreviations are the same as in Fig. 6. This sounding was launched in the center of the IOR.

An IOR was deployed surrounding the cold front north of Dodge City near Ness City, Kansas (box in Fig. 3). Although only cumuli developed along the cold front in the IOR during the deployment, deep convection was initiated along the cold front just west of the IOR. An M-GLASS sounding taken within 5 km from the initiation location about 90 min prior to initiation (Fig. 6) shows little difference from the sounding taken within the grid domain an hour later (Fig. 5). Because the superadiabatic layer is so shallow, and because the soundings have a history of inaccurate surface temperature readings, a parcel path based on the surface temperature may underestimate the amount of CIN present. Therefore, for the 2044 UTC sounding, a parcel with the mean CBL temperature at 1200 m AGL plus one standard deviation (to capture the effects of thermals) recorded by the King Air ahead of the cold front was used for the CIN, LCL, and LFC calculations in Fig. 5. Aircraft data were not available near the 1935 UTC sounding, so a parcel with a CBL temperature recorded by the sounding at approximately 1200 m plus the standard deviation recorded by the King Air was used for the calculations in Fig. 6. Both soundings indicate small amounts of CIN, and neither is obviously more favorable than the other for initiating convection.

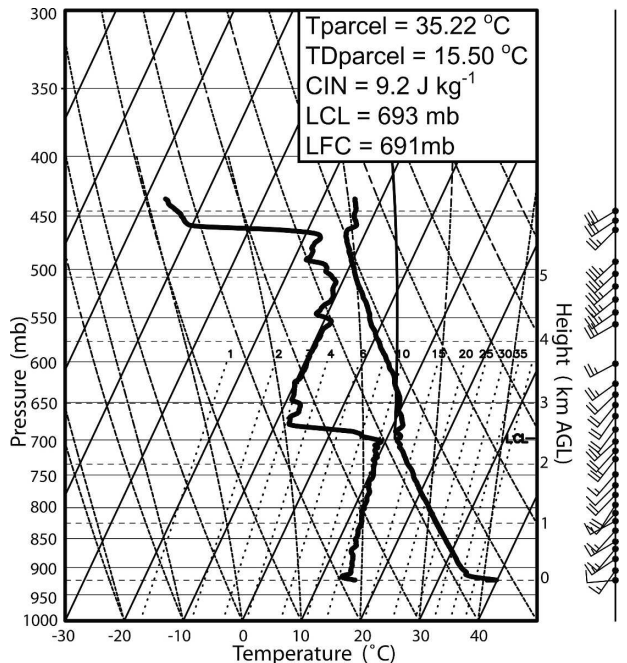
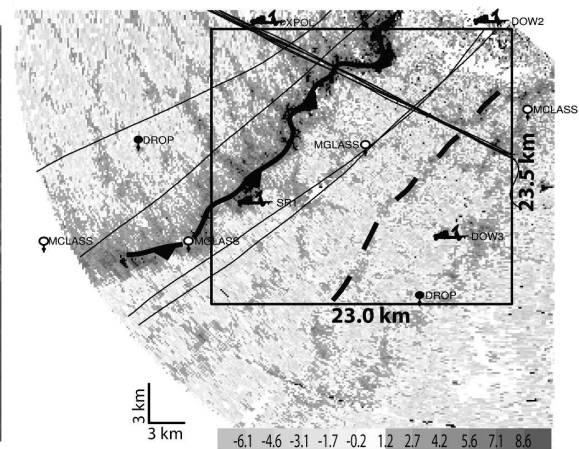
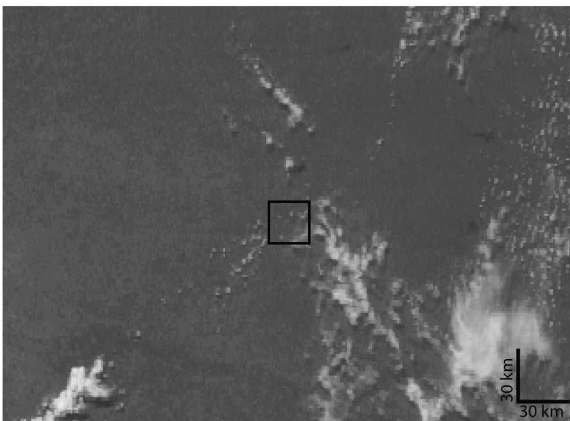
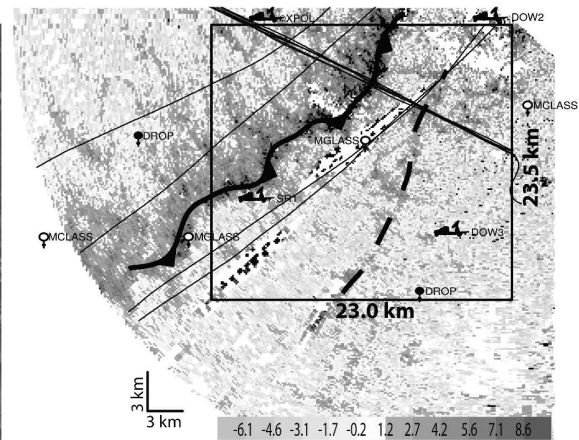
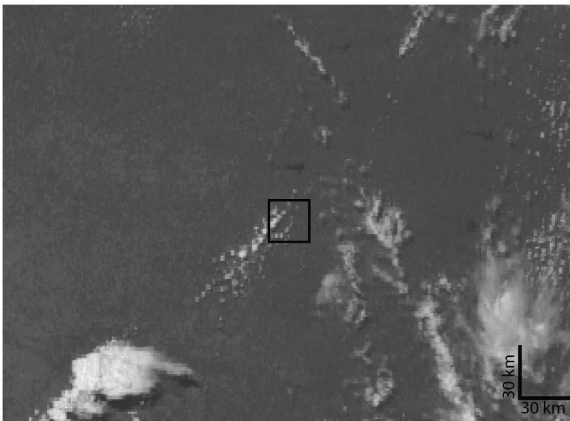


FIG. 6. Sounding on skew T for M-GLASS1 at 1935 UTC. Full wind barb is 10 kt; half barb is 5 kt. The parcel path and calculated indices are shown for a parcel with a surface temperature of 35.22°C (T_{parcel}) and the surface dewpoint temperature observed by the sounding (TD_{parcel}). This sounding was launched approximately 5 km from where convection was initiated.

a) 1934 UTC



b) 2003 UTC



c) 2020 UTC

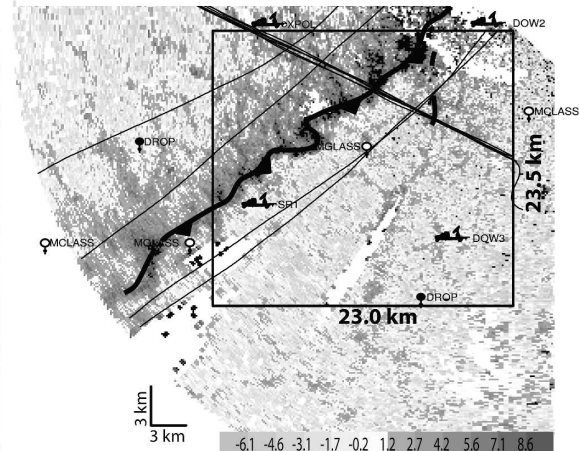
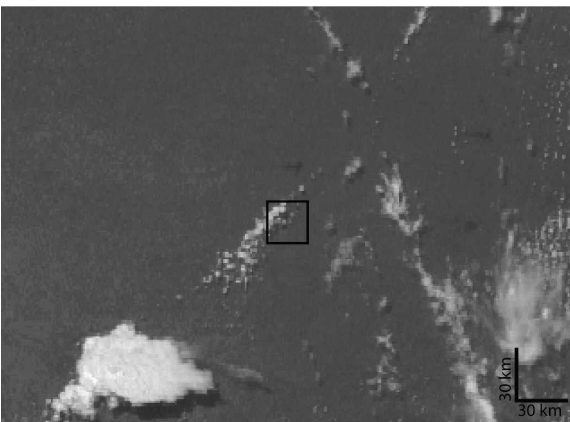
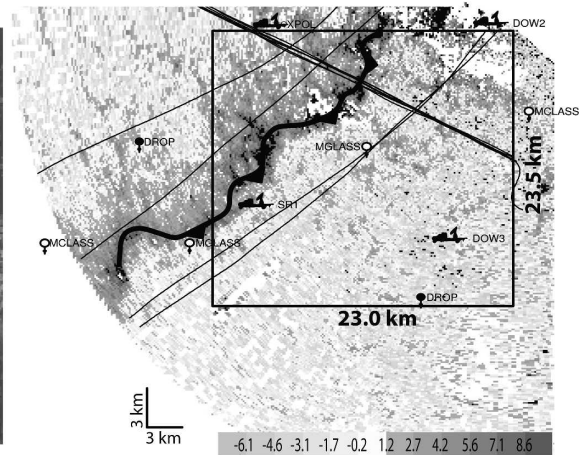
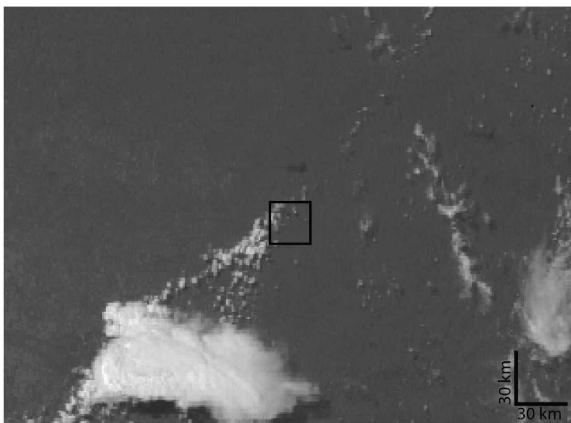
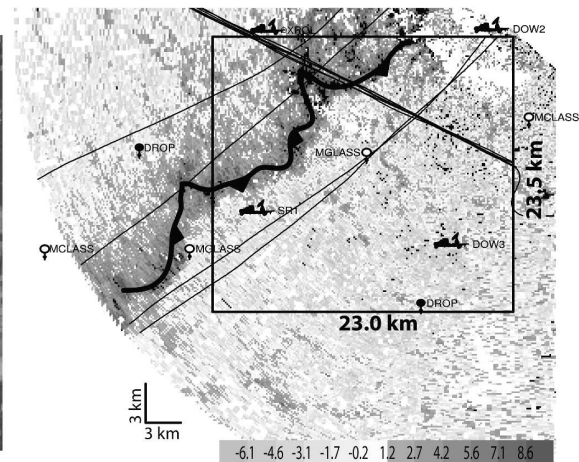
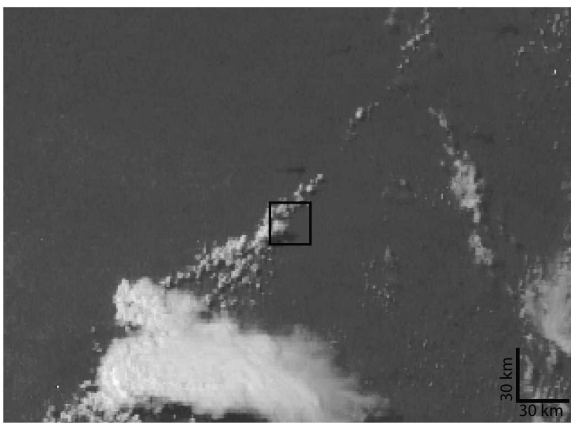


FIG. 7. Time series of (left) 1-km visible satellite and (right) base (0.5°) reflectivity (dBZ) from DOW2. Missing radar data are shaded white. The black box represents the grid domain (IOR) in subsequent analyses. The solid lines are the aircraft tracks as indicated in Fig. 1. The location of the cold front, based solely on DOW2 reflectivity, is denoted using conventional symbols. Likewise, the secondary thin line is denoted with the dashed line.

d) 2045 UTC



e) 2103 UTC



f) 2121 UTC

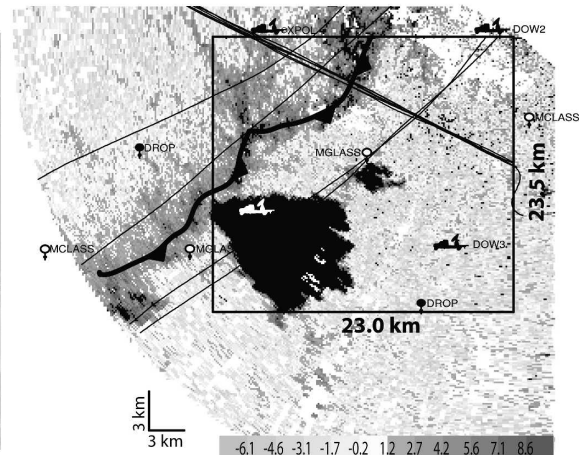


FIG. 7. (Continued)

b. Kinematic structure of the front

Scientists with DOW2 and DOW3 noted widely scattered cumulus humilis during the first 30 min of the deployment on 10 June 2002. These are also evident in the 1-km visible satellite imagery (Fig. 7a). At this time,

DOW2 detected a reflectivity thin line indicative of the cold front and a secondary, weaker line to its east. Smaller, weaker reflectivity maxima are present west of the front. By 2000 UTC, cumulus towers were developing in the IOR while the two thin lines approached each other (Fig. 7b). The clouds grew in size and num-

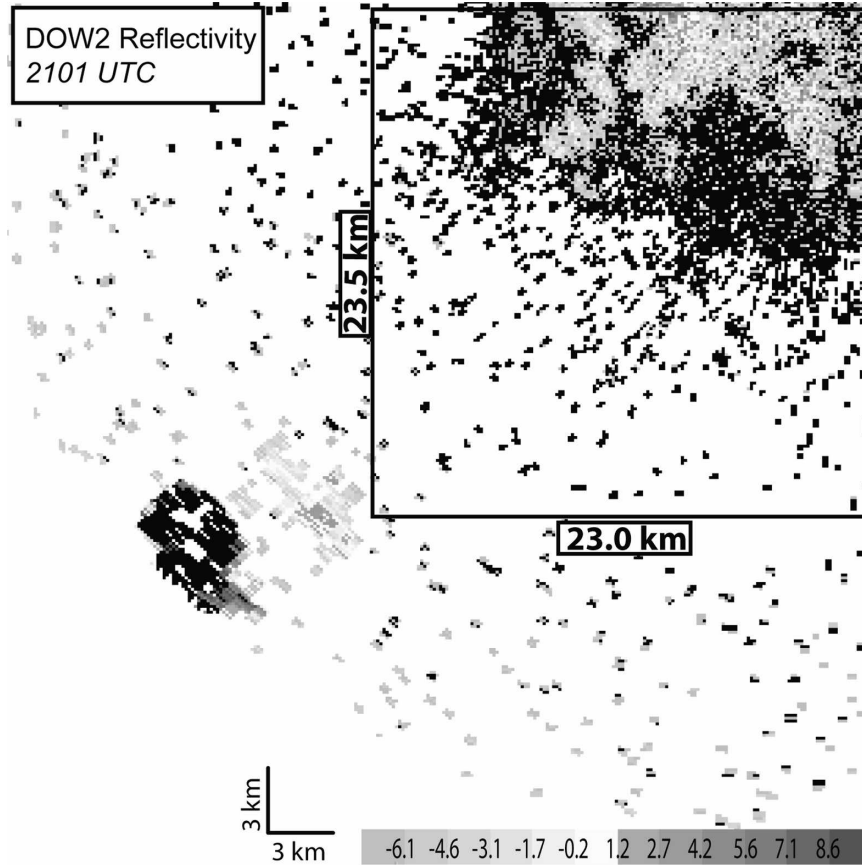


FIG. 8. DOW2 reflectivity at 9.4°. The black box indicates the IOR. Enhanced reflectivity southwest of the IOR is the convection that was initiated at 2103 UTC.

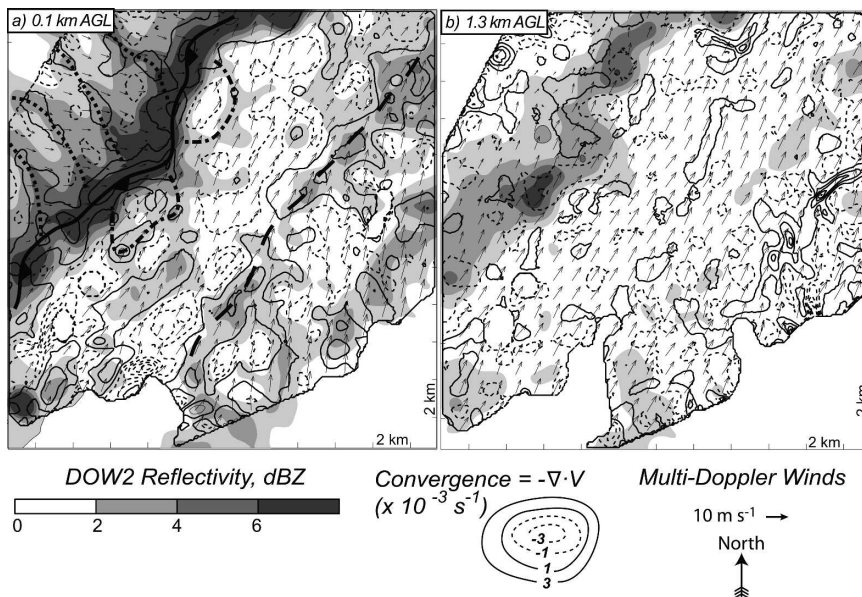


FIG. 9. DOW2 reflectivity with multi-Doppler synthesized winds and convergence at 1946 UTC over the entire IOR: (a) 0.1 and (b) 1.3 km AGL. Convergence is contoured every $2 \times 10^{-3} \text{ s}^{-1}$. The cold front is marked with conventional symbols. Short dashed lines indicate the upward branches of LRMs behind the cold front, and dash-dot curves indicate open-cell convection just ahead of the cold front. The long dashed line is the secondary convergence zone.

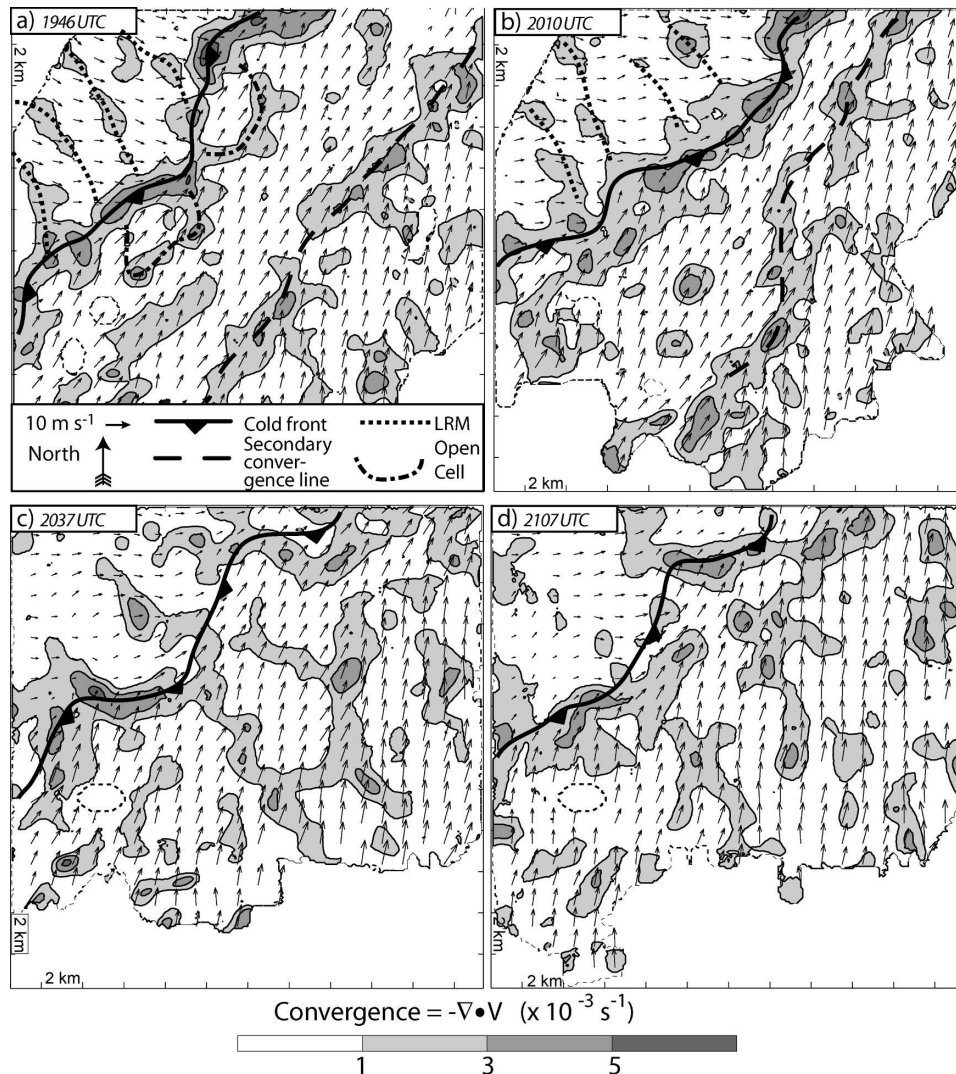


FIG. 10. Multi-Doppler syntheses at 100 m AGL showing how convergence becomes more discontinuous along the cold front. (a), (b) Contributions of three radars; (c), (d) contributions of four radars. The center time of the volume is indicated in the top-left corners. Horizontal wind vectors are plotted every 10 grid points (1 km). White circles surrounded by dashed lines indicate areas of missing data.

ber along the front as indicated by the clouds filling in along the cold front in the satellite imagery (Fig. 7c) until 2030 UTC when they became widely scattered (Fig. 7d). Simultaneously, the cold front thin line became more diffuse and the secondary thin line moved north out of the IOR. By 2103 UTC, however, towering cumulus clouds redeveloped in the southwest corner of the IOR and deep convection was initiated just outside of the IOR. Even though the base reflectivity from DOW2 does not show any sign of initiation at this time, upper-level reflectivity maxima indicative of rain formation in the growing cumulus clouds at 5.7 km AGL were first observed at 2055 UTC on the edge of the DOW2 9.4° scan (Fig. 8). Indeed, by 2121 UTC, the

base radar reflectivity confirms that convection had been initiated and the fully developed storm with reflectivities nearing 50 dBZ entered the IOR (Fig. 7f). Similarly, the small cell just north of the main storm initiated on the edge of the DOW2 scans.

Multi-Doppler syntheses at 0.1 and 1.3 km AGL illustrate the finescale structure of the convergence and horizontal wind fields associated with the cold front, linear reflectivity maxima west of the front, and secondary thin line (Fig. 9). The domain shown in Fig. 9 and in subsequent radar synthesis figures is the entire IOR unless otherwise noted. As expected, convergence maxima typically coincide with reflectivity maxima. The reflectivity thin line, enhanced convergence, and a wind

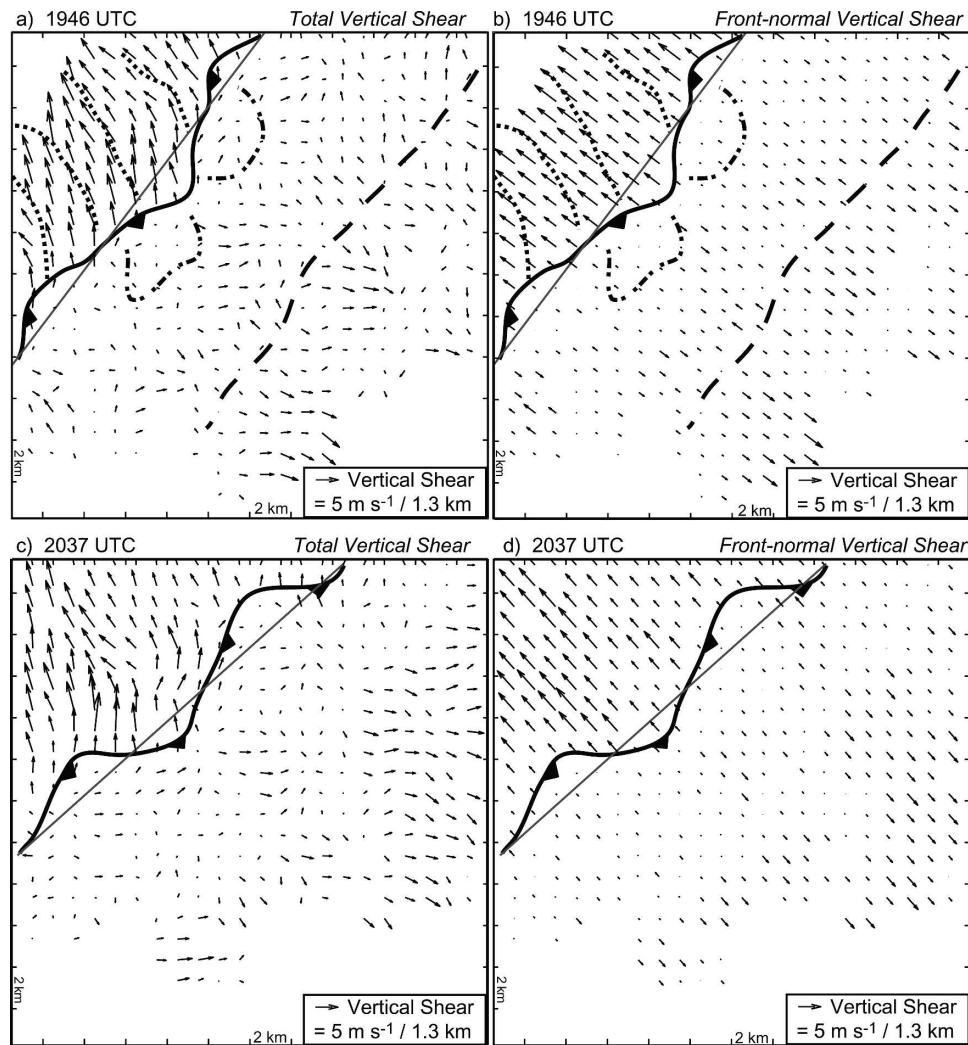


FIG. 11. (left) Total vertical wind shear between 0.1 and 1.4 km AGL and (right) the front-normal component of the vertical wind shear between 0.1 and 1.4 km AGL at (top) 1946 and (bottom) 2037 UTC. The gray oblique line represents the two-dimensional front orientation used to calculate the front-normal component of the shear vectors. The other symbols are the same as in previous figures.

shift mark the cold front position. In addition, four linear reflectivity and convergence maxima behind and roughly perpendicular to the front (Fig. 9a) resemble HCRs in that convergence weakens with height (Fig. 9b) up to the top of our domain, suggesting their circulation may encompass the depth of the boundary layer. Further, these features align with the boundary layer vertical wind shear (shown later), as Ferrare et al. (1991) note. Unlike some previous studies on HCRs, however, the observed features do not align with the mean boundary layer wind; indeed the mean boundary layer wind is nearly perpendicular to these features (not shown). Perhaps some discrepancy exists because the vertical shear is predominantly speed shear in the studies where HCRs align with the mean wind, while on 10

June 2002, and in the case of Ferrare et al. (1991), the vertical shear has a directional component that may lead to a closer alignment between HCRs and the shear vector.

These reflectivity maxima may alternately be explained as reflections in the boundary layer of gravity waves in the weak capping inversion aloft. The estimated Brunt-Väisälä frequency (N) in this inversion layer is 0.02 s^{-1} . Using

$$c = \frac{\lambda N}{2\pi}, \quad (2)$$

where λ is the horizontal spacing of the features (3 km) gives a phase speed (c) of 9.6 m s^{-1} . These features appear to move little, and the wind speed and direction in the stable layer is 10 m s^{-1} at 213° . Hence, if these

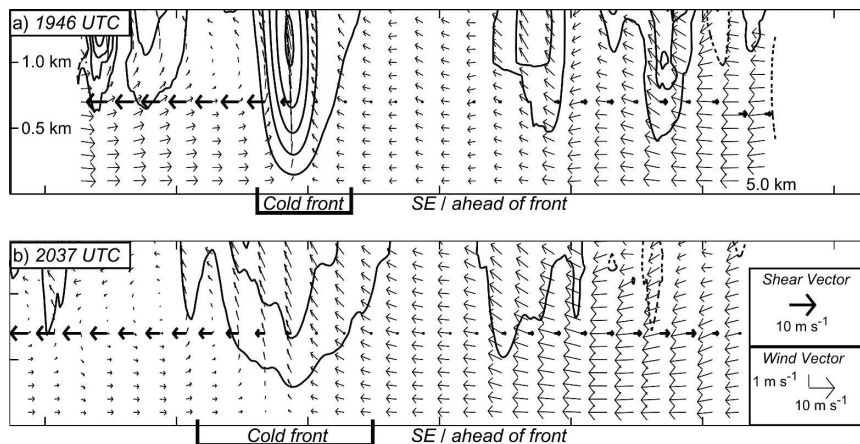


FIG. 12. Average vertical velocity contoured every 0.5 m s^{-1} (solid contours positive, dashed contours negative, 0 m s^{-1} contour not shown) in the plane of the average cross section across the cold front. The wind vectors and the vertical shear vectors are in the vertical plane that approximates the two-dimensional orientation of the cold front (thin oblique lines in Fig. 11). Vectors are plotted every 10 data points. The vertical scale is in km AGL.

features are propagating with a phase speed of 9.6 m s^{-1} from the northeast, little net movement would result. HCRs in the boundary layer could be a source of the gravity waves, possibly making these features a reflection of gravity waves and HCRs. Unfortunately, no data are available through these features above the boundary layer to confirm the presence of gravity waves in the capping inversion. Thus, because we cannot diagnose with certainty the origins of these linear reflectivity and convergence maxima, we will refer to them from hereon as linear reflectivity maxima (LRMs).

Reflectivity and convergence rings ahead of the cold front indicative of the observed open-cell convection also are evident (Fig. 9a). The secondary thin line observed in the raw reflectivity fields is present in the multi-Doppler syntheses as a convergence line with a south to southwest wind shift across it.

Near the upper boundary of the multi-Doppler domain (Fig. 9b), the convergence and reflectivity signatures are weaker and the wind direction varies less across the location of the surface cold front and secondary convergence line. Further, there is less evidence of the LRMs in the reflectivity field as the low-level convergence has been replaced by divergence at this level. Although divergence indicates some weakening of the vertical velocity with height, positive vertical velocity extends to the top of the domain over the LRMs, the cold front, the secondary convergence line, and the boundary layer convective cells.

c. Evolution of convergence along the front

The along-line variability of the depth and strength of convergence along the cold front at this time are

extraordinary. To complicate matters, the cold front and boundary layer structure also varied significantly in time. Normally, such transient and small-scale features might not be trusted, but the fine spatial and temporal resolution, volume-to-volume temporal continuity, and favorable comparisons with aircraft data validate their existence. Convergence at 100 m AGL for four different times is shown in Fig. 10. Figure 10a is similar to Fig. 9a except without DOW2 reflectivity. At this time, convergence is evident along the entire length of the cold front. Note, however, that convergence along the cold front and secondary boundary is spatially variable with local maxima embedded in the background field. Between the two boundaries is a region of divergence. As the two convergence zones approach each other (Fig. 10b), the LRMs remain well defined, but the open-cell convection becomes less distinct and the divergent region between the two zones becomes smaller.

By 2037 UTC (Fig. 10c), however, convergence along the cold front becomes markedly fractured. High temporal resolution reflectivity imagery (not shown) indicate that most of the secondary convergence line was advected by the southerly mean flow out of the IOR. The LRMs and open-cell convection also are less distinct. Finally, when deep convection is initiated just west of the IOR (Fig. 10d), the convergence field is more continuous than at 2037 UTC, but less so than at 2010 UTC. Reasons for the observed changes in convergence are discussed in the next section.

d. Evolution of the frontal circulation

We now consider why the upward motion pattern was more fractured after 2020 UTC than before. Ver-

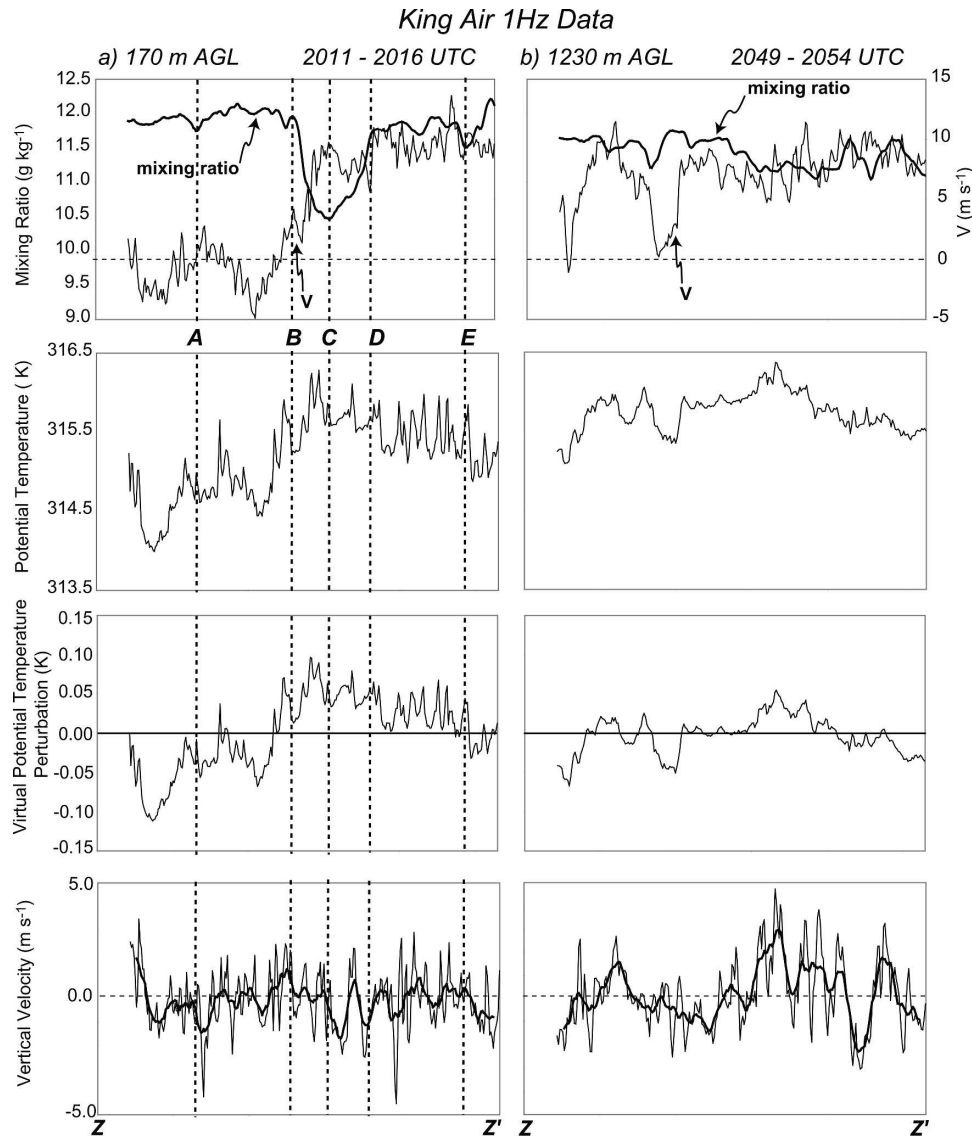


FIG. 13. Data recorded at 1 Hz from the Wyoming King Air at (a) 170 and (b) 1230 m AGL. The points in (a) refer to locations in Fig. 14. The data are along the path indicated by Z-Z' in Fig. 1. The thick black line on the vertical velocity plots is a 10-s running mean.

tical wind shear in the IOR indicates a horizontal vorticity imbalance across the front (Fig. 11). Here vertical wind shear is defined as the difference between the wind vector at 1.4 km AGL and the wind vector at 100 m AGL. The orientation of the cold front is approximated by the thin oblique lines in order to calculate a front-normal shear vector. To attain the optimal vorticity balance of RKW theory (Rotunno et al. 1988), the front-normal shear vectors ahead of the front should have the same magnitude, but opposite direction, as those behind the front. This balance clearly is not present at most locations along the front during the deployment (Fig. 11), indicating that this front may not

provide optimal lifting and that updrafts will tilt back over the front.

To assess the evolution of the frontal circulation as a whole, a coordinate transformation is performed such that the new x' axis (x') is roughly parallel to the cold front and the new y' axis (y') is perpendicular to the cold front. Horizontal winds are also transformed such that u is along x' and v is along y' . Using a piecewise function to approximate the front, u , v , and w were averaged along the front. The averaging reduces the data to only the y' and z dimensions, yielding an average vertical cross section across the front (Fig. 12). It is clear in these cross sections that the vertical shear be-

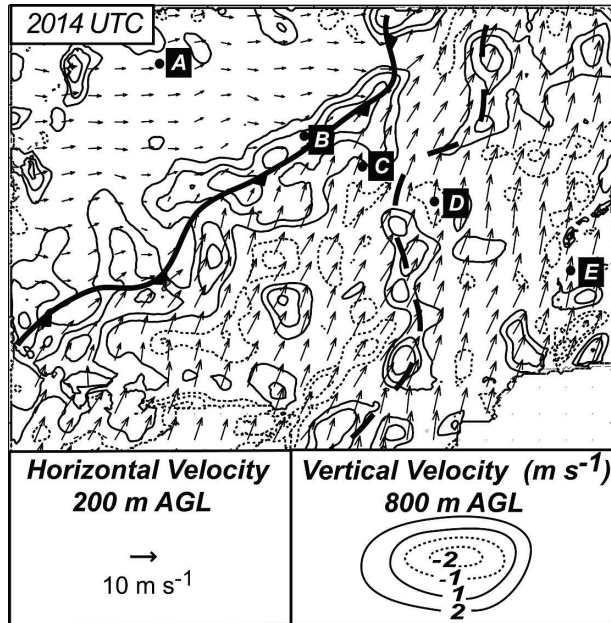


FIG. 14. Points along the King Air flight track between 2011 and 2016 UTC at 170 m AGL relative to vertical velocity along the front. Vectors are spaced every 1 km. The letters are referred to in the text.

tween 1.4 and 0.1 km AGL ahead and behind the front are unbalanced. Average upward motion associated with the cold front is much stronger at 1946 UTC (Fig. 12a) than that at 2037 UTC (Fig. 12b). Reasons for this weakening in time are addressed in the next section.

e. Thermodynamic structure and evolution of the front

The University of Wyoming King Air flew across the cold front at several elevations between 2010 and 2103 UTC. Data at an average of 170 m AGL (905 mb) and 1230 m AGL (803 mb) [standard deviations of height

AGL (pressure) are 14 m (3 mb) and 33 m (1 mb), respectively] are shown in Figs. 13a and 13b, respectively. The north–south component of the wind (V) indicates clearly the location of the cold front at 170 m AGL (point B), which agrees with the multi-Doppler synthesis frontal location (Fig. 14). The significant minimum in mixing ratio (point C), is likely caused by downward vertical motion advecting dry air from higher in the boundary layer (Figs. 13a and 14), and is likely transient in time because it is not evident at upper levels on a later pass (Fig. 13b). Although potential temperature is about 1°C less behind the front than ahead of it, mixing ratio is slightly higher behind the front. Virtual potential temperature perturbations are negative west of the cold front and are positive east of the cold front (Fig. 13c). Furthermore, the virtual potential temperature perturbations decrease and become negative east of the secondary convergence line (between points D and E) indicating that this convergence line is associated with density gradient.

To explore reasons why the cold front weakened, we turn to the frontogenesis equation, which is given by

$$F = \frac{D}{Dt} |\nabla_p \theta| \tag{3}$$

(Bluestein 1993), where θ is potential temperature. For an overall estimate of frontogenesis on 10 June 2002, we assume no variations in the x direction (perpendicular to the path of the King Air). Furthermore, $(\partial\theta/\partial z) \approx 0$ in the nearly dry adiabatic boundary layer. Equation (3) then simplifies to

$$F = \frac{\partial v}{\partial y} \frac{\partial \theta}{\partial y} + \text{diabatic terms}, \tag{4}$$

where v is the wind component along y (in this case, along the King Air path). Using the 170 m AGL data from the King Air valid between 2011 and 2016 UTC,

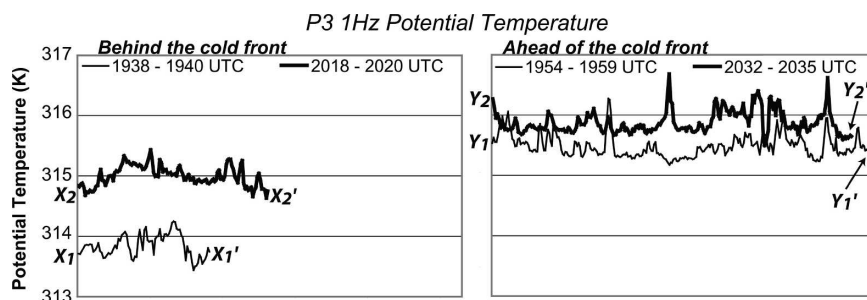


FIG. 15. P-3 1-Hz data showing enhanced warming behind the (left) cold front compared to the (right) ahead of the fold front. X–X' (etc.) indicate the P-3 track in Fig. 1 during which the data were collected. Two traverses are shown for both ahead and behind the front at approximately 600 m AGL, as indicated in Fig. 1.

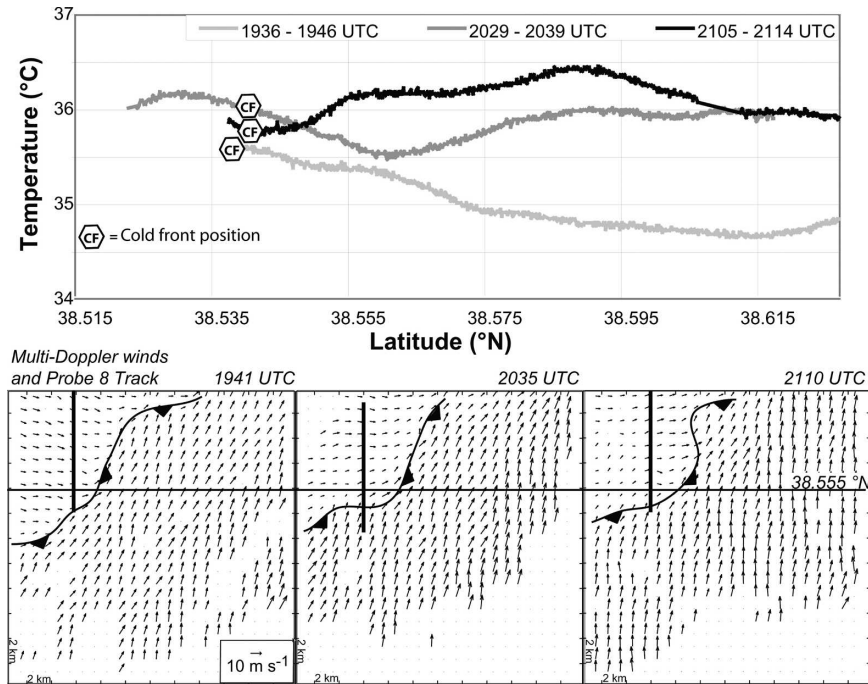


FIG. 16. Temperature recorded by mobile mesonet probe 8 showing warming behind the cold front. (top) Temperature vs latitude for three times. (bottom) Probe 8 track (vertical line) and multi-Doppler winds valid during the track for the three times shown in the top panel. Horizontal line through the synthesis is the location of 38.555°N , also marked in the top panel.

the first term is $2.3^{\circ}\text{C h}^{-1} \text{ km}^{-1}$. This term is positive, as expected due to convergence along the front. The average vertical cross sections across the front, however, indicate a weakening of the frontal circulation with time; therefore, the diabatic terms must be negative.

To verify the sign of the diabatic terms, data from the P-3 are examined. The P-3 flew parallel to the front, twice behind it and twice ahead of it (Fig. 1). Data were collected at 550 m AGL (on average) and are shown in Fig. 15. During its flight behind the front between 1938 and 1940 UTC, the average potential temperature was 313.85 K (Fig. 15, left panel, thin line), while ahead of the front between 1954 and 1959 UTC the average potential temperature was 315.48 K (Fig. 15, right panel, thin line), indicating a 1.63-K drop in potential temperature across the boundary, similar to data collected by the King Air.

The next flight behind the boundary (2018–2020 UTC) indicates an average 1.51-K increase in potential temperature (Fig. 15, left panel, thick line) compared to the flight behind the boundary 40 min earlier. Ahead of the front, the average potential temperature increased only 0.40 K (Fig. 15, right panel, thick line).

This warming behind the front also was observed at the surface by a mobile mesonet probe (Fig. 16). Data for three passes along the same longitude are shown.

For each pass, the cold front was just south of 38.555°N . Although there are few data points ahead of the front, warming behind the front in time is clear, with an average 1.1°C increase, similar to that observed by the P-3. This warming behind the cold front is represented in the diabatic heating term of F , and is frontolytic. Hence, the weakening frontal circulation we observe in Fig. 12 is likely caused by the enhanced warming behind the cold front.

f. Structure and evolution of vertical velocity and vertical vorticity

In addition to temporal and spatial variability in convergence, the cold front also displayed significant variations in vertical velocity and in vertical vorticity (Fig. 17) over this time period. As expected, convergence along the cold front (Fig. 10a) indicates rising motion aloft (Fig. 17a). Vertical velocity along the secondary convergence line is generally weaker than that along the cold front. Rising motion associated with the LRMs and open-cell convection is also evident.

The horizontal wind shear across the cold front (see the wind vectors in Fig. 10) is associated with a zone of positive ζ along the cold front (Fig. 17). In contrast, very little vertical vorticity is present along the secondary convergence line. Four striking ζ maxima (misocyc-

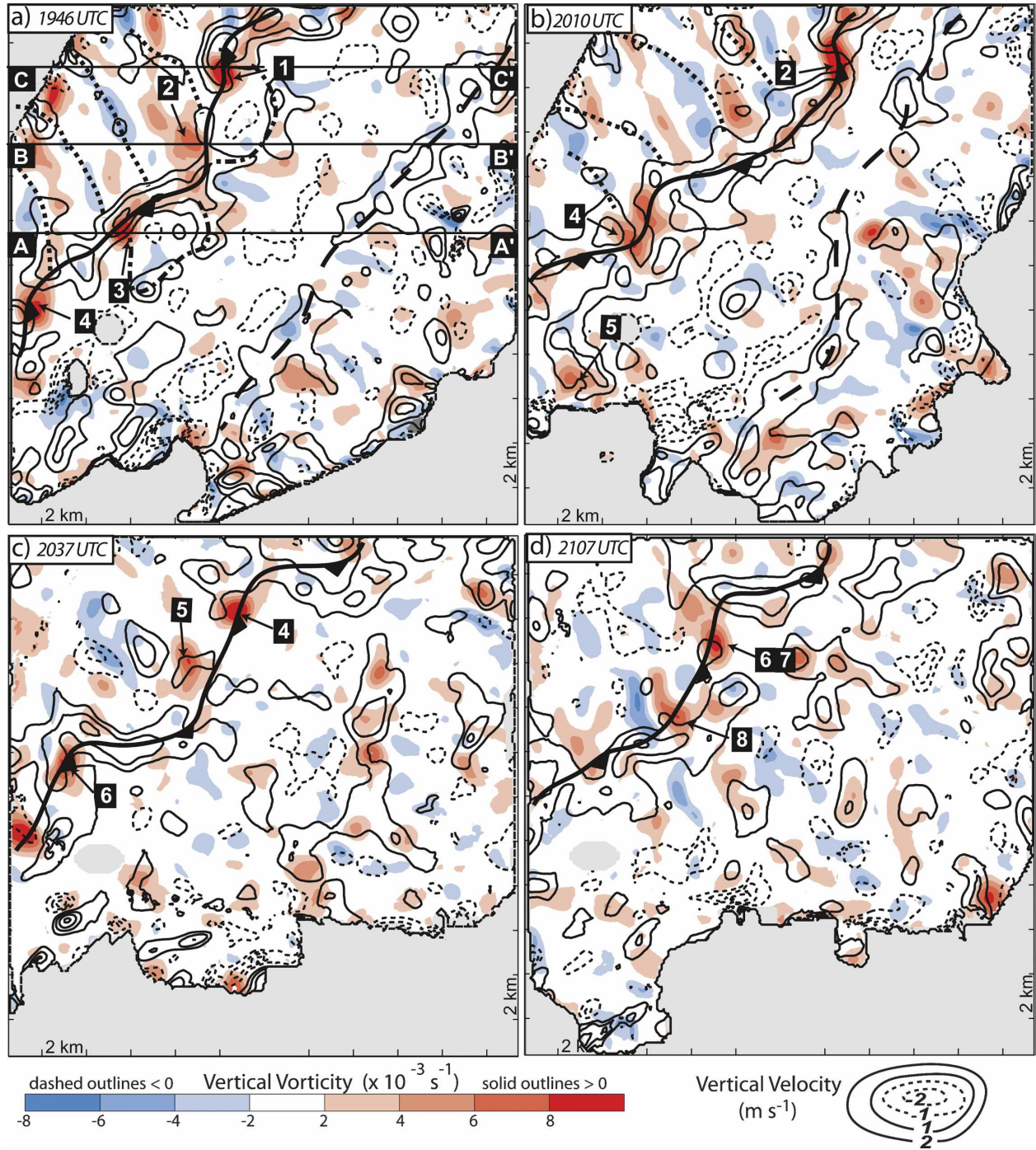


FIG. 17. Vertical velocity and vertical vorticity at 0.8 km AGL at (a) 1946, (b) 2010, (c) 2037, and (d) 2107 UTC. Cold front and other symbols are the same as in Fig. 10. Numbers indicate individual misocyclones discussed in the text. Lines in (a) are cross sections referred to in the text and in Fig. 18. Upward motion is nearly continuous along the front in (a) and (b), but becomes discontinuous in (c) and (d). Gray shading indicates regions of missing data.

clones) are present along the front at this time. All four misocyclones are near an intersection of an LRM with the cold front, similar to Wilson et al. (1992) and Atkins et al. (1995). Furthermore, as also noted by previous

researchers, the w maxima along the cold front typically occur in association with, but offset from, a misocyclone (e.g., Kingsmill 1995; Lee and Wilhelmson 1997). For instance, in the case of misocyclones 1 and 3, the w

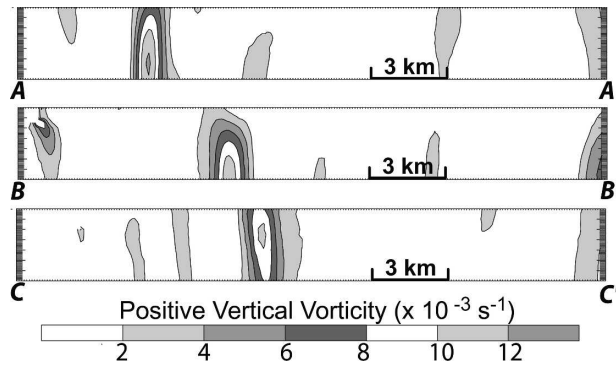


FIG. 18. Positive vertical vorticity at 1946 UTC along the cross sections shown in Fig. 17 showing the vertical structure of misocyclones. The vertical scale spans the depth of the domain (0.0 to 1.4 km) and is stretched by a factor of 2.

maximum is northwest of the misocyclone, whereas for misocyclones 2 and 4, the w maximum is due north of the misocyclone.

Vertical cross sections of misocyclones 1, 2, and 3 reveal that the misocyclones are deep features, extending at least to the top of the domain (Fig. 18). For misocyclones 1 and 3, ζ is maximized above the lowest radar elevation indicating that the vorticity may be produced through tilting. Near the surface, ζ in the misocyclones is stronger than the ambient ζ along the cold front suggesting the importance of stretching in this region. Computing the vorticity tendency terms along trajectories through a misocyclone may help clarify the origins of the misocyclones and will be addressed in a future paper.

The evolution of w and ζ is similar to that of convergence. At 1946 UTC (Fig. 17a), four misocyclones are present along the cold front, but $+w$ is fractured only slightly (between misocyclones 1 and 2 and near misocyclone 4). At 2010 UTC, the convergence lines approached each other and the number of misocyclones along the front decreased. Misocyclone 2 has intensified, but it is aligned along the front, and does not break the upward motion pattern significantly. On the other hand, misocyclone 4 has created a kink in the boundary. The only break in upward motion along the front at this time is over this kink. Misocyclone 3 dissipated and misocyclone 1 propagated out of the IOR. Notice that upward motion is more continuous along the front at this time than at other times.

Starting at 2020 UTC, several misocyclones begin to merge, and the axes of the mergers tend to be perpendicular to the front. Much like a vortex sheet rolling up, several significant kinks in reflectivity (not shown) develop as a consequence of these misocyclones (Marquis et al. 2004), coincident with large fractures of upward

motion along the cold front (Fig. 17c). This continues until the end of the deployment when a very large merger of misocyclone 6 with ζ associated with LRMS behind the cold front creates an occluded appearance in the reflectivity field (not shown) and a large kink and break in upward motion along the cold front (Fig. 17d).

g. Parcel trajectories and evolution of cumulus clouds

Parcel trajectories are computed to estimate how the evolution of convergence and upward motion affect the cumulus field. At two different times, parcels at 100 m AGL are chosen every 1 km in a region straddling the cold front (Figs. 19a and 19b). The parcels are traced forward and backward in time over the entire period they are in the IOR. Parcels entering the frontal circulation have strong along-frontal components to their motion. During the first hour of the deployment, parcels entering the convergence zone ascend along a mostly vertical path (Fig. 20a), but after 2020 UTC, many fewer parcels leave the top of the domain (Fig. 20b).

The decrease in the number of parcels able to exit the top of the domain is directly related to the fractured pattern of upward motion along the cold front that results from the superposition of the weakening front and embedded misocyclones. For instance, when upward motion along the cold front is nearly continuous, parcels entering the frontal zone retain upward motion as they move horizontally along the front, allowing the parcels to rise for a long period of time. When the upward motion becomes discontinuous, however, parcels moving along the cold front enter regions of varying vertical forcing, causing them to rise initially, but then to decelerate, and possibly even descend, as they encounter regions of downward forcing. If, however, parcels move with the same speed as the w maximum, they may also reach the top of the domain. Vertical velocity maxima associated with misocyclones tend to have this trait even if w is not continuous along the boundary and may, therefore, be preferred locations for initiation when upward motion is discontinuous. The w maximum associated with misocyclone 6 is an example of such a location. Parcels chosen at 100 m AGL in enhanced convergence associated with misocyclone 6 retain upward forcing as the misocyclone moves along the front (Figs. 19c and 19d). Therefore, for maximum parcel displacement, parcels must remain in regions of upward forcing for a significant time by either moving through a region with continuous upward forcing or by moving at the same velocity as a maximum in upward forcing.

The discontinuous upward motion along the weak-

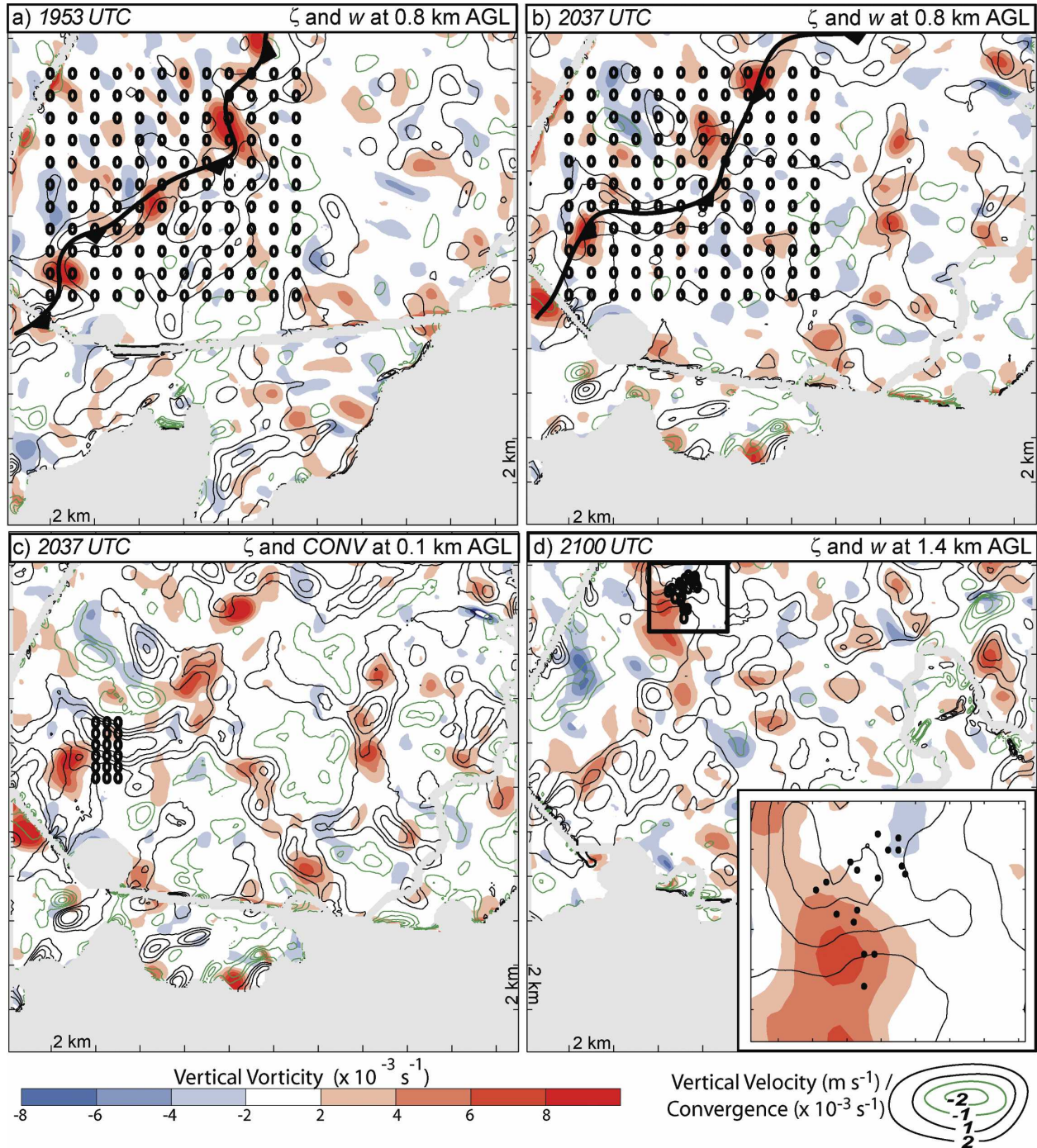


FIG. 19. (a), (b) Locations of parcels at 100 m AGL (denoted by circles) chosen for trajectories shown in Fig. 20. (c) Locations of parcels at 100 m AGL in upward motion associated with misocyclone 6. Note that convergence is contoured instead of vertical velocity because vertical velocity is nearly zero at 100 m AGL. (d) Location of parcels in (c) when they reach the top of the domain. The location of the inset is denoted by the black box. Gray shading indicates regions of missing data.

ened cold front causes the cumulus cloud field to become scattered and more shallow as well. Cumulus congestus clouds deepen along the cold front between 2000 and 2015 UTC (Fig. 21a). At 2020 UTC (Fig. 21b),

the viewing angle of the northernmost camera changes, focusing on the northernmost portion of the cold front where clouds tended to be more shallow. Hence, it is unclear if the clouds become more shallow

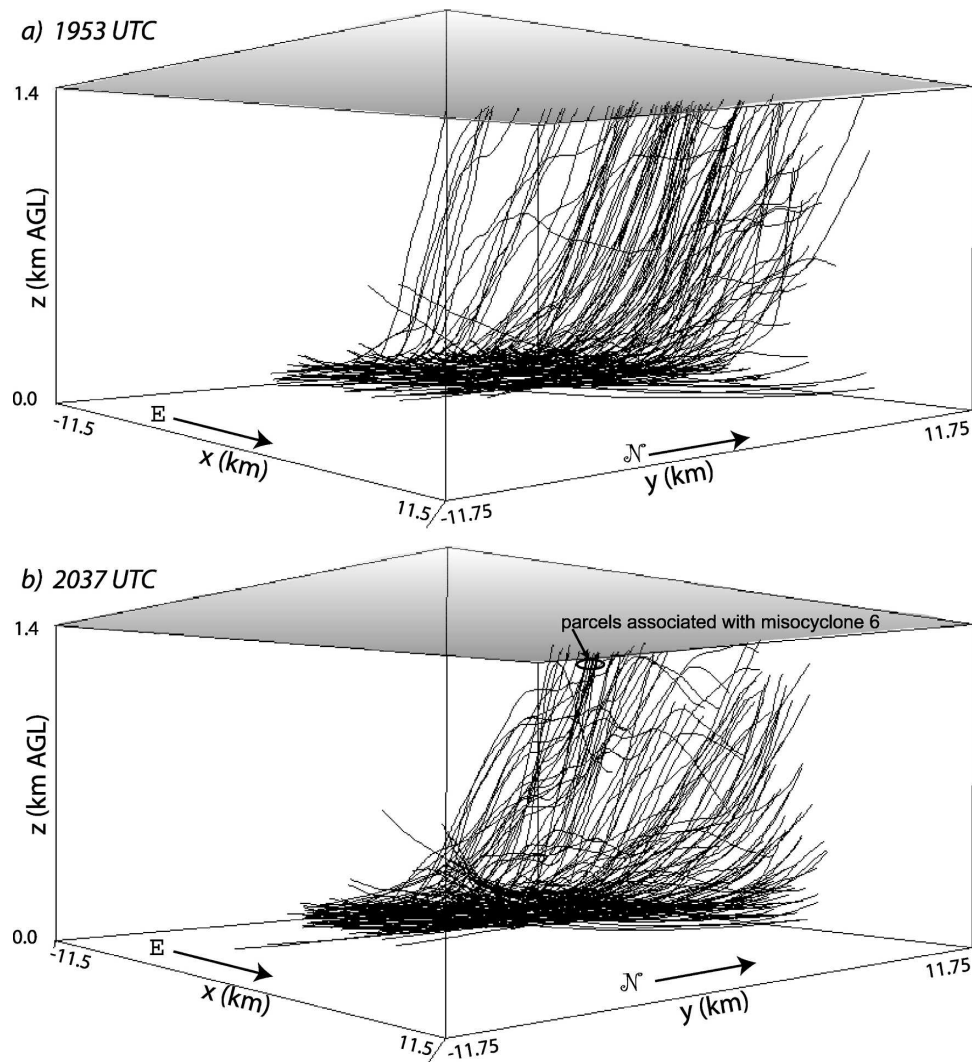


FIG. 20. Trajectories looking northwest toward the cold front. Parcels not intersecting the top of the domain exit the domain through one of the sides (usually the north side). All parcels were chosen at 100 m AGL and the trajectories trace the path the parcel took before and after the time indicated. (a) Parcels were chosen at 1953 UTC and traced back in time to 1928 UTC and forward in time to 2043 UTC when all parcels had exited the domain. (b) Parcels were chosen at 2037 UTC and traced back in time to 2010 UTC and forward in time to 2118 UTC when all parcels had exited the domain. The vertical lines correspond to the corners of the grid box. Notice that more parcels reach the top of the domain in (a) than in (b).

between 2015 and 2020 UTC, or if the apparent decrease in cloud depth is due to the change in the viewing angle. Nevertheless, between 2020 and 2037 UTC, the cumulus clouds clearly become more shallow (Fig. 21c).

Photogrammetric analyses (Rasmussen et al. 2003) of the cloud fields indicate a decrease in areal coverage of the cumulus clouds (Fig. 22). Cloud bases are contoured assuming an LCL of 3 km. Note that w and ζ are shown 10 min prior to the time of the cloud analysis. This is to account for the fact that parcels at the level

shown in a $2\text{--}3\text{ m s}^{-1}$ updraft at the top of the domain require approximately 10 min to travel the additional 2.2 km to cloud base. Thus, we expect the cloud evolution to lag the w evolution by about 10 min. Grid cells in which 50% or more pixels contain cloud base are contoured. It must be noted that although these analyses indicate only where there are definitely clouds, regions outside the 50% contour do not necessarily indicate a lack of clouds. For instance, clouds may block each other from the camera view, cloud base may be indistinct, or the clouds may be too distant to determine

a) 2015 UTC
Cumulus congestus
clouds along the
northern portion of
the cold front.



b) 2020 UTC
Viewing angle
focuses more
toward the north.



c) 2037 UTC
Cumulus clouds
are more scattered
and more shallow.



FIG. 21. Photographs of cumulus clouds along the cold front. The camera is the northernmost of the two in Fig. 22.

cloud base. Despite this caveat, the photogrammetric analyses are supported by 1-km visible satellite imagery showing similar dissipation in cloud coverage, and scientists with DOW2 and DOW3 noted this dissipation in their visual observations during the deployment.

Thus, the weakened front and resulting discontinuous upward motion after 2020 UTC diminish the areal coverage and depth of cumulus clouds along the cold front because parcels traveling along the cold front experience less dwell time in regions of upward forcing.

Nevertheless, scattered cumulus clouds remain. These clouds likely are associated with the w maxima that advect with the flow (e.g., maxima associated with the misocyclones) such that parcels retain upward motion. For instance, misocyclone 6 is associated with strong vertical motion, and trajectories in this region show that parcels in this upward motion reach the top of the domain (Fig. 20b). Unfortunately, misocyclone 6 was outside the cloud photogrammetry domain, but visible satellite imagery does indicate a cloud near this area.

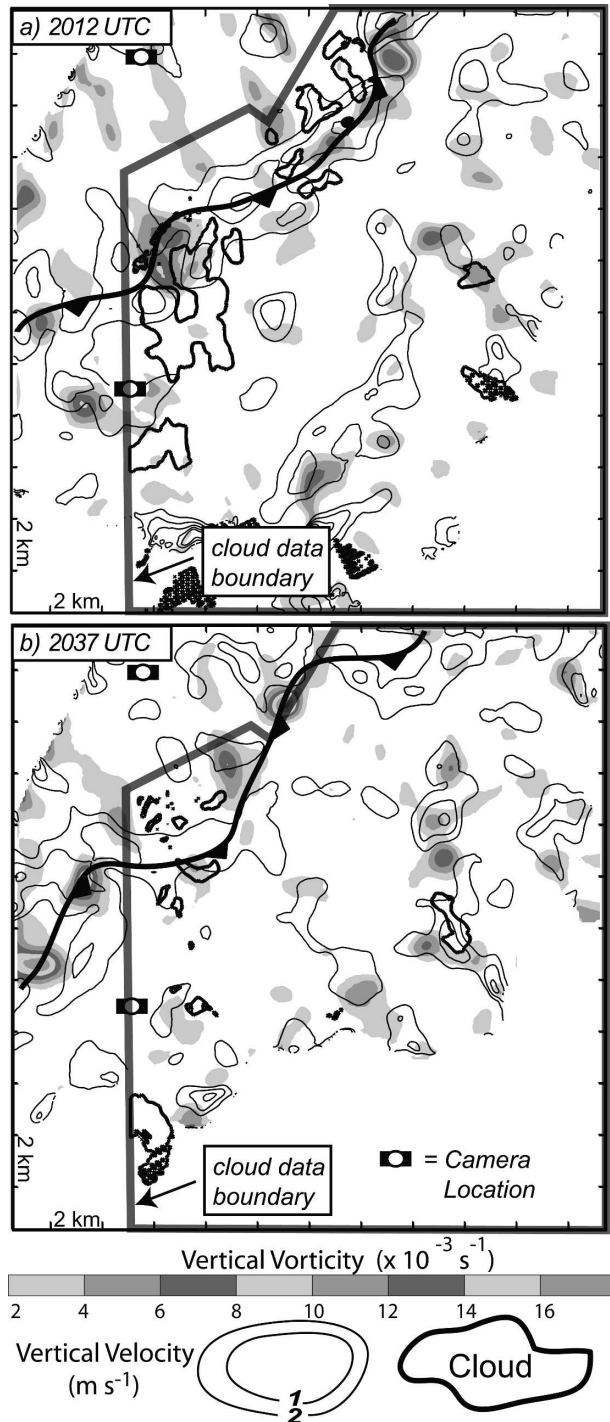


FIG. 22. Photogrammetric analysis of the cloud field illustrating the decrease in the areal extent of the cumulus cloud field. Note only positive w and z are contoured at 0.8 km AGL for clarity. The times correspond to the w and z fields; the clouds are plotted 10 min later than this time to account for the ~ 10 min excursion parcels take from 0.8 km AGL to cloud base.

4. Discussion and conclusions

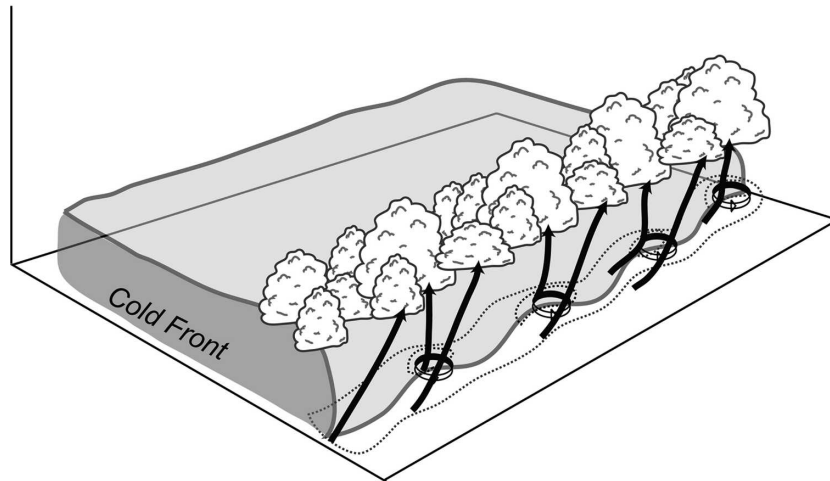
High spatial and temporal resolution overdetermined dual-Doppler syntheses, thermodynamic data, and cloud images were examined to explain the evolution of a cold front and cumulus clouds along it. Because the mobile radars were able to deploy close to the cold front, they collected data with spatial resolution significantly finer than in previous CI studies. Furthermore, the temporal resolution is 90 s. These high spatial and temporal resolution analyses reveal in detail the cold front, LRMs, open-cell convection, misocyclones, and a second convergence boundary. Further, this high resolution allows us to compute parcel trajectories, uncommon in past CI studies.

This study highlights the response of a cumulus cloud field to a weakening frontal circulation in the presence of strong miso-scale features (misocyclones). This response is summarized in a schematic in Fig. 23. Between 1946 and 2020 UTC, upward motion is nearly continuous along the cold front (Fig. 23a). At this time, small-scale features such as misocyclones create embedded w maxima, but the cold front is the dominant mechanism in organizing upward motion in a continuous swath along the front. Parcels entering and translating along the cold-frontal convergence zone remain in regions of upward forcing, and hence are able to reach the LFC. As a result, cumulus clouds develop along the cold front.

Later, differential diabatic heating causes the cold-frontal circulation to weaken. As a result, upward motion along the cold front decreases and smaller-scale features such as misocyclones have greater influence on organizing the overall pattern of vertical velocity (Fig. 23b). This weakening frontal circulation superimposed with misocyclones leads to discontinuous upward motion along the front, with the location and strength of upward motion changing as misocyclones evolve, merge, and propagate along the front. Parcels entering the convergence zone no longer translate through a continuous swath of upward forcing. Instead, many parcels experience varying upward and downward displacements, and consequently, they do not reach the LCL. Further cloud development along the front is hindered, and many existing cumulus clouds dissipate in the dry air above the boundary layer. Some vertical velocity maxima, such as those sometimes associated with misocyclones, however, move with a velocity similar to that of the parcels and maintain their strength as they move. Parcels in such fortuitous circumstances may reach the LCL.

In many past studies, misocyclones have been favorable locations for cloud development (Wilson et al.

- a) Misocyclones create small kinks and w maxima, but upward motion is continuous along the front.



- b) As the cold front weakens, misocyclones severely distort the front and upward motion is fractured, but they continue to be associated with w maxima.

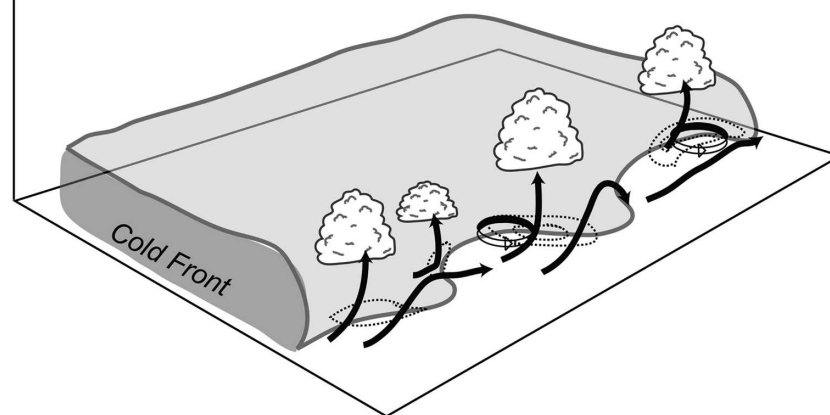


FIG. 23. Schematic summarizing the effects of misocyclones on the cold front and on the cumulus clouds on 10 Jun 2002. Upward motion is contoured; misocyclones are indicated by circles with arrows, and bold lines with arrows represent example trajectories. (a) Upward motion is continuous along the front and misocyclones are associated with w maxima. Parcels rise with an alongfront horizontal component except near misocyclones where parcel motion is nearly vertical. (b) Misocyclones have created large kinks in the front, resulting in fractured upward motion along the front. Fewer parcels retain upward motion for long periods and some may even descend (negative w not contoured). Parcels remaining in the favorable region associated with misocyclones, however, still rise to cloud base.

1992; Atkins et al. 1995). In the present case, misocyclones are also favored regions for lifting. Most misocyclones are associated with a nearby w maximum (e.g., Wilson et al. 1992; Atkins et al. 1995; Kingsmill 1995; and this study), and, in some cases, the w maximum advects with the misocyclone without substantial changes in strength and orientation, allowing parcels to retain the enhanced upward motion and to ascend sig-

nificantly. Hence, these are favorable regions for cloud development or growth.

The height of the LFC likely is key to the difficulty in initiating convection as well. Had the LFC been lower, parcels would have required less time with upward motion to attain their LFC, and the discontinuous nature of upward forcing would have less impact. The same is true if w along the front was stronger. Perhaps this has

been a reason for the conflicting analysis of the role of misocyclones in CI in previous studies.

Kinematic data extending to the top of the boundary layer, as well as increased resolution in the thermodynamic data, would assist in determining why, despite the presence of towering cumulus clouds and enhanced vertical motion associated with misocyclones, deep convection was not initiated in the IOR. It is possible that the vertical motion was not sufficient in sustaining the clouds against entrainment in the dry air above the boundary layer.

One then asks: Given the frontolysis in the IOR, how did a severe storm develop along the front 5 km away from the IOR? In the region where convection was initiated, some mechanism may have provided locally prolonged intense moisture convergence to deepen the moist layer or there may have been considerable along-line variability in midlevel moisture, which is not likely based on the soundings in the IOR compared with those near the location where convection initiated and based on lidar data (D. E. Kingsmill 2004, personal communication). Movies of visible satellite imagery show that a mesoscale cloud line south of the IOR intersected the cold front where convection was initiated. Perhaps this boundary provided the moisture convergence necessary for CI. Unfortunately, aircraft operations in that area ended just prior to initiation, so no definitive conclusions can be drawn.

This study has demonstrated that identifying misocyclones along a convergence boundary may be important in forecasting cloud development, particularly during periods in which they dominate the vertical velocity pattern. Furthermore, knowing the steadiness of the vertical velocity maxima associated with the misocyclones may be key in determining whether those vertical velocity maxima will be associated with parcels reaching the LCL or LFC. This suggests that data with resolution much finer than is currently possible operationally are required to pinpoint if and where along a convergence boundary (in the absence of boundary intersections) convection will initiate. As many previous studies have pointed out, higher-resolution thermodynamic data would be useful in addressing the remaining questions in this study and in forecasting cloud development along a convergence zone.

Acknowledgments. Paul Markowski provided several computer codes for plotting and analyzing the data presented in this paper. This paper benefitted from comments by Bart Geerts, Jim Wilson, Katja Friedrich, Paul Markowski, Ken Davis, Tammy Weckwerth, Justin Arnott, David Kingsmill, Cyrille Flamant, and Jim Marquis. Robert Hart wrote the GrADS code that plot-

ted the soundings. Curtis Alexander provided the interface to the binary radar data. Conrad Ziegler's assistance with the SMART-Radar data is appreciated. We thank Bart Geerts for use of the King Air data. We are grateful for the effort and cooperation of all the scientists who participated in IHOP. Finally, we thank Jeff Hutton of the Dodge City, Kansas, NWS Office for his help with determining camera locations for the photogrammetric analyses.

This work was supported by an American Meteorology Society Graduate Fellowship sponsored by ITT Industries, a National Science Foundation Graduate Research Fellowship, and National Science Foundation Grants ATM-0208651, ATM-0131325, and ATM-0336712.

REFERENCES

- Arnott, N. R., Y. P. Richardson, and J. M. Wurman, 2003: A solar alignment technique for determining mobile radar pointing angles. Preprints, *31st Conf. on Radar Meteorology*, Seattle, WA, Amer. Meteor. Soc., 492–495.
- Atkins, N. T., R. M. Wakimoto, and T. M. Weckwerth, 1995: Observations of the sea-breeze front during CaPE. Part II: Dual-Doppler and aircraft analysis. *Mon. Wea. Rev.*, **123**, 944–969.
- Bargen, D. W., and R. C. Brown, 1980: Interactive radar velocity unfolding. Preprints, *17th Conf. on Radar Meteorology*, Seattle, WA, Amer. Meteor. Soc., 278–283.
- Barnes, S. L., 1964: A technique for maximizing details in numerical weather map analysis. *J. Appl. Meteor.*, **3**, 396–409.
- Biggerstaff, M. I., and J. Guynes, 2000: A new tool for atmospheric research. Preprints, *20th Conf. on Severe Local Storms*, Orlando, FL, Amer. Meteor. Soc., 277–280.
- Bluestein, H. B., 1993: *Synoptic-Dynamic Meteorology in Midlatitudes*. Vol II. Oxford University Press, 594 pp.
- Byers, H. R., and H. R. Rodebush, 1948: Causes of thunderstorms of the Florida peninsula. *J. Meteor.*, **5**, 275–280.
- Fankhauser, J. C., N. A. Crook, J. Tuttle, L. J. Miller, and C. G. Wade, 1995: Initiation of deep convection along boundary layer convergence lines in a semitropical environment. *Mon. Wea. Rev.*, **123**, 291–313.
- Ferrare, R. A., J. L. Schols, and E. W. Eloranta, 1991: Lidar observations of banded convection during BLX83. *J. Appl. Meteor.*, **30**, 312–326.
- Hane, C. E., H. B. Bluestein, T. M. Crawford, M. E. Baldwin, and R. M. Rabin, 1997: Severe thunderstorm development in relation to along-dryline variability: A case study. *Mon. Wea. Rev.*, **125**, 231–251.
- , R. M. Rabin, T. M. Crawford, H. M. Bluestein, and M. E. Baldwin, 2002: A case study of severe storm development along a dryline within a synoptically active environment. Part II: Multiple boundaries and convective initiation. *Mon. Wea. Rev.*, **130**, 900–902.
- Kessinger, C. J., P. S. Ray, and C. E. Hane, 1987: The Oklahoma squall line of 19 May 1977. Part I: A multiple Doppler analysis of convective and stratiform structure. *J. Atmos. Sci.*, **44**, 2840–2864.
- Kingsmill, D. E., 1995: Convection initiation associated with a sea-breeze front, a gust front, and their collision. *Mon. Wea. Rev.*, **123**, 2913–2933.

- Koch, S. E., M. desJardins, and P. J. Kocin, 1983: An interactive Barnes objective map analysis scheme for use with satellite and conventional data. *J. Climate Appl. Meteor.*, **9**, 1487–1503.
- Lee, B. D., and R. B. Wilhelmson, 1997: The numerical simulation of non-supercell tornadogenesis. Part I: Initiation and evolution of pretornadic mesocyclone circulations along a dry outflow boundary. *J. Atmos. Sci.*, **54**, 32–60.
- , R. D. Farley, and M. R. Hjelmfelt, 1991: A numerical case study of convection initiation along colliding convergence boundaries in northeast Colorado. *J. Atmos. Sci.*, **48**, 2350–2365.
- Marquis, J. N., Y. P. Richardson, and J. M. Wurman, 2004: Observations of mesocyclones along boundaries during IHOP. Preprints, *22d Conf. on Severe Local Storms*, Hyannis, MA, Amer. Meteor. Soc., CD-ROM, 16A.5.
- Matejka, T., 2002: Estimating the most steady frame of reference from Doppler radar data. *J. Atmos. Oceanic Technol.*, **19**, 1035–1048.
- Oye, R., and M. Case, 1995: REORDER—A program for gridding radar data: Installation and use manual for the UNIX version. NCAR, 22 pp. [Available from Field Observing Facility, National Center for Atmospheric Research, P.O. Box 3000, Boulder, CO 80307.]
- , C. Mueller, and S. Smith, 1995: Software for radar data translation, visualization, editing, and interpolation. Preprints, *27th Conf. on Radar Meteorology*, Vail, CO, Amer. Meteor. Soc., 359–361.
- Parsons, D., T. Weckwerth, and M. Hardesty, 2001: Scientific overview document for the International H₂O Project. Version 2.1, NCAR, 44 pp.
- Pauley, P. M., and X. Wu, 1990: The theoretical, discrete, and actual response of the Barnes objective analysis scheme for one- and two-dimensional fields. *Mon. Wea. Rev.*, **118**, 1145–1163.
- Rasmussen, E. N., R. P. Davies-Jones, and R. L. Holle, 2003: Terrestrial photogrammetry of weather images acquired in uncontrolled circumstances. *J. Atmos. Oceanic Technol.*, **20**, 1790–1803.
- Rotunno, R., J. Klemp, and M. L. Weisman, 1988: A theory for strong, long-lived squall lines. *J. Atmos. Sci.*, **45**, 463–485.
- Weaver, J. F., and S. P. Nelson, 1982: Multiscale aspects of thunderstorm gust fronts and their effects on subsequent storm development. *Mon. Wea. Rev.*, **110**, 707–718.
- Weckwerth, T. M., and R. M. Wakimoto, 1992: The initiation and organization of convective cells atop a cold-air outflow boundary. *Mon. Wea. Rev.*, **120**, 2169–2187.
- , J. W. Wilson, and R. M. Wakimoto, 1996: Thermodynamic variability within the convective boundary layer due to horizontal convective rolls. *Mon. Wea. Rev.*, **124**, 769–784.
- , and Coauthors, 2004: An overview of the International H₂O Project (IHOP_2002) and some preliminary highlights. *Bull. Amer. Meteor. Soc.*, **85**, 253–277.
- Wilson, J. W., and W. E. Schreiber, 1986: Initiation of convective storms at radar-observed boundary-layer convergence lines. *Mon. Wea. Rev.*, **114**, 2516–2536.
- , and D. L. Meegenhardt, 1997: Thunderstorm initiation, organization, and lifetime associated with Florida boundary layer convergence zones. *Mon. Wea. Rev.*, **125**, 1507–1525.
- , G. B. Foote, N. A. Crook, J. C. Fankhauser, C. G. Wade, J. D. Tuttle, and C. K. Mueller, 1992: The role of boundary-layer convergence zones and horizontal rolls in the initiation of thunderstorms: A case study. *Mon. Wea. Rev.*, **120**, 1785–1814.
- , T. M. Weckwerth, J. Vivekanandan, R. M. Wakimoto, and R. W. Russell, 1994: Boundary layer clear-air radar echoes: Origin of echoes and accuracy of derived winds. *J. Atmos. Oceanic Technol.*, **11**, 1184–1206.
- Wurman, J., 2001: The DOW mobile multiple Doppler network. Preprints, *30th Int. Conf. on Radar Meteorology*, Munich, Germany, Amer. Meteor. Soc., 95–97.
- , J. Straka, E. Rasmussen, M. Randall, and A. Zahrai, 1997: Design and development of a portable, pencil-beam, pulsed, 3-cm Doppler radar. *J. Atmos. Oceanic Technol.*, **14**, 1502–1512.
- Ziegler, C. L., and E. N. Rasmussen, 1998: The initiation of moist convection at the dryline: Forecasting issues from a case study perspective. *Wea. Forecasting*, **13**, 1106–1131.
- , T. J. Lee, and R. A. Pielke Sr., 1997: Convective initiation at the dryline: A modeling study. *Mon. Wea. Rev.*, **125**, 1001–1026.